

# Simulation of Thermal and Electrical Transport in Nanotube and Nanowire Composites

Satish Kumar, Muhammad A. Alam and Jayathi Y. Murthy

**Abstract** Nanotube-based thin-film composites promise significant improvement over existing technologies in the performance of large-area macroelectronics, flexible electronics, energy harvesting and storage, and in bio-chemical sensing applications. We present an overview of recent research on the electrical and thermal performance of thin-film composites composed of random 2D dispersions of nanotubes in a host matrix. Results from direct simulations of electrical and thermal transport in these composites using a finite volume method are compared to those using an effective medium approximation. The role of contact physics and percolation in influencing electrical and thermal behavior are explored. The effect of heterogeneous networks of semiconducting and metallic tubes on the transport properties of the thin film composites is investigated. Transport through a network of nanotubes is dominated by the interfacial resistance at the contact of two tubes. We explore the interfacial thermal interaction between two carbon nanotubes in a crossed configuration using molecular dynamics simulation and wavelet methods. We pass a high temperature pulse along one of the nanotubes and investigate the energy transfer to the other tube. Wavelet transformations of heat pulses show that

---

S. Kumar (✉)

G. W. Woodruff School of Mechanical Engineering, Georgia Institute of Technology,  
Atlanta, GA 30332, USA  
e-mail: satish.kumar@me.gatech.edu

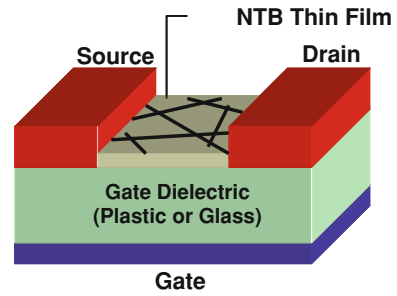
M. A. Alam

School of Electrical and Computer Engineering, Purdue University,  
West Lafayette, IN 47097, USA  
e-mail: alam@ecn.purdue.edu

J. Y. Murthy

School of Mechanical Engineering, Purdue University,  
West Lafayette, IN 47097, USA  
e-mail: jmurthy@ecn.purdue.edu

**Fig. 1** Schematic of nanotube network thin-film transistor showing source, drain, gate and channel region composed of nanotube composite



how different phonon modes are excited and how they evolve and propagate along the tube axis depending on its chirality.

## 1 Introduction

In recent years, there has been enormous interest in fabricating thin-film transistors (TFTs) on flexible substrates in the rapidly growing field of large-area macro-electronics [1, 2]. Applications include displays [1], e-paper, e-clothing, pressure-sensitive skin [3, 4], large-area chemical and biological sensors [5, 6], flexible and shape-conformable antennae and radar, as well as intelligent and responsive surfaces with large-area control of temperature, drag and other properties [2]. Flexible substrates such as plastic require low temperature processing, typically below 200°C. Prevailing technologies such as amorphous silicon (a-Si) and organic TFTs can be processed at low temperature and are sufficient for low-performance applications such as displays, where their low carrier mobility ( $\sim 1\text{--}10\text{ cm}^2/\text{Vs}$ ) [4, 7] is not a limitation. For high-performance applications, however, the choices are limited. Single crystal silicon CMOS and polycrystalline silicon (poly-Si) technologies can yield higher performance, but are expensive and cannot be fabricated below 250°C. Nanotube-bundle (NTB) based TFTs, consisting of carbon nanotubes (CNTs) dispersed in substrates such as polymer and glass, are being explored to substantially increase the performance of flexible electronics to address *medium-to-high performance* applications in the 10–100 MHz range [2]. High mobility, substrate-neutrality and low-cost processing make NTB-TFTs very promising for these flexible-electronics applications.

Two distinct classes of materials are being pursued by researchers [8–11]. On the one hand, *randomly-oriented* nanotubes embedded in polymer have been used to fabricate nanotube network thin-film transistors (NNT-TFTs) which promise relatively high carrier mobility ( $\sim 100\text{ cm}^2/\text{Vs}$ ). Here, solution-processing is used to disperse a random network of CNTs in a plastic substrate, as shown in Fig. 1, to form a thin film. The mat of CNTs forms the channel region of the transistor. Because NNT-TFTs do not require precise alignment of CNTs, they are amenable to mass manufacture, and are relatively inexpensive. A number of groups have fabricated and analyzed these TFTs for macro-electronic and chemical sensing

applications [7, 8] and have begun to explore their performance. Snow et al. reported the mobility and conductance properties of carbon nanotube (CNT) networks and also explored the interfacial properties of CNTs in chemical sensors [9–11]. Menard et al. fabricated thin film transistors on plastic substrates using nano-scale objects (microstrips, platelets, disks, etc.) of single crystal silicon. Zhou et al. demonstrated fabrication of p-type and n-type transistors [8], which could be used as building blocks for complex complementary circuits. Fabrication of an integrated digital circuit composed of up to nearly 100 transistors on plastic substrates using random network of CNTs has been reported by Cao et al. [12]. Other experimental reports on CNT TFT fabrication can be found in [2, 12, 13]. A number of groups have focused on developing TFTs with *well-aligned* and *or partially-aligned* nanotubes for very high performance applications [14–16] using transfer printing; mobilities of 1,000 cm<sup>2</sup>/Vs, comparable to single-crystal silicon are achievable using this technology.

Though there has been a great deal of research on composites, [17– 20] nanocomposites for use in macroelectronics pose very specific problems. First, unlike most published research on 3D transport in composites, our interest is in 2D thin-film composites in which in-plane electrical transport dominates, and in which in-plane thermal spreading plays a central role in determining device temperature. Furthermore, macroelectronic devices are typically of the 1–50 micron scale. At these scales, the nanotube length may compete with the finite size of the device, and unlike in most published research, bulk composite behavior does not obtain. Furthermore, there remain a large number of unknowns regarding the ultimate performance limits of NTB-TFTs. For example, nearly all reported work has concentrated on device fabrication and processing, but little is understood about the fundamental physics that govern device operation and scaling as a function of tube orientation, tube density, ratio of metallic to semiconducting tubes, and tube-substrate interaction [21].

Strong electrical, thermal and optical interactions between the tubes and between the tubes and the substrates affect device performance, but there has been little fundamental work to explore these interactions quantitatively. Furthermore, metallic CNTs form 30% of typical NNTs which are problematic because they can short source and drain and limit on–off ratios [22]. Recently, a number of techniques for removing them have been reported. A gas-phase plasma hydrocarbonation reaction technique has been reported to selectively etch and gasify metallic nanotubes and obtain pure semiconducting nanotubes [23]. Another process that separates single-walled carbon nanotubes (SWNTs) by diameter, band gap and electronic type using centrifugation of compositions has been reported by Arnold et al. [24]. The degree to which metallic tubes can influence on/off ratios must be understood for controlled and optimal design. Last but not least, the supply voltage used thus far in driving these devices has been untenably high, leading to unacceptable power dissipation and hysteresis due to charge injection. Processing conditions must be optimized to reduce the supply voltage to acceptable values.

**Table 1** Experimental results for enhancement in effective thermal conductivity of CNT composites

Composite type	Diameter (d)(nm)	Length ( $L_t$ )	Concentration (%)	Increase in $k_{eff}$ (%) over substrate	Network (type)
SWNT/Silicon elastomer [66]	–	–	3.8 wt	65	Random
SWNT/Epoxy [27]	1.1	–	1 wt	125	Random
SWNT/Epoxy [57]	1.1	170 nm	1 wt	80	Random
MWNT/Carbon [67]	20–40	10–100 $\mu\text{m}$	–	12.31	Aligned
MWNT/Silicon elastomer [25]	12	0.3 mm	0.4 vo	280	Aligned
MWNT/Oil [68]	25	50 $\mu\text{m}$	1 vol	160	Random
MWNT/Water [69]	20–60	>10 $\mu\text{m}$	0.84 vo	27.3	Random

The electrical performance of NNT-TFT macroelectronics could be severely compromised by self-heating. Cooling options are limited if macroelectronics are to be kept flexible. A temperature rise above ambient in the 100°C range is expected for passive natural convection cooling and is expected to scale linearly with frequency and quadratically with drain voltage. High temperatures not only compromise electrical performance but also have consequences for the thermo-mechanical reliability of flexible substrates. An inability to control self-heating would mean either employing lower-speed TFTs or decreasing the number of transistors per unit area. It is therefore necessary not only to understand thermal transport in these composites, but the interaction of electrical and thermal transport in determining device performance and reliability.

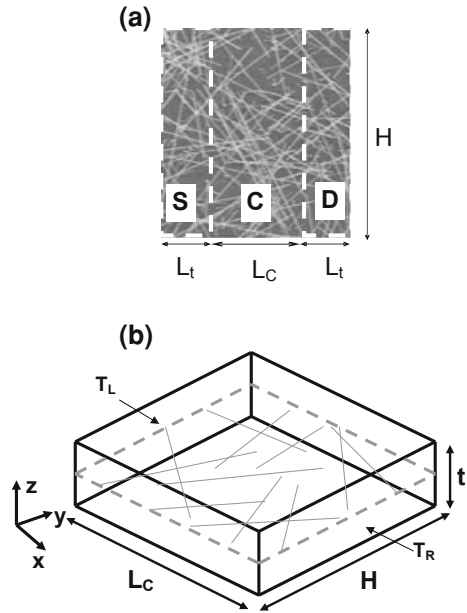
Low density CNT composites have been extensively explored for applications in thermal management [25–27], and high strength materials [28, 29]. In these applications, CNTs are embedded in host substrate as a random matrix. A percolating network of CNTs is found to be formed even at low volume fractions ( $\sim 0.2\%$ ) due to their high aspect ratio [27, 30]. Theoretical and numerical studies based on the effective medium approximation (EMA) [18, 26], Monte-Carlo simulations [31] or scaling analysis [32] have been reported on percolating nanotube networks or their composites to predict their effective electrical or thermal transport properties. However, many of these studies significantly limit the thermal conductivity ratios addressed and do not address finite-sized 2D composites. A number of experimental measurements of effective thermal conductivity ( $k_{eff}$ ) of nanotube suspensions in either substrates or fluids have been reported recently, and are summarized in Table 1. There are large disparities in the reported enhancement of  $k_{eff}$  over that of the substrate. However, all experiments show that the maximum achievable conductivity is less than three times that of the underlying matrix/fluid, a harbinger of thermal problems in NNT-TFTs. It is necessary to understand and control the physics underlying these performance limits, particularly the influence of tube–tube and tube-substrate contact parameters on  $k_{eff}$ .

A firm understanding of tube–tube and tube-substrate interfacial transport may provide guidelines for improving the efficiency and reliability of CNT based devices. Various experimental and numerical studies have been performed to estimate the thermal conductivity of CNTs and also to measure the thermal resistance between the CNT and the substrate. Most numerical studies are based on the molecular dynamics (MD) method [33, 34]. A list of these studies may be found in Lukes and Jhong [33]. Small et al. measured the tube-to-substrate resistance (on a per-length basis) of 12 Km/W for a MWNT supported on a substrate [35] and Maune et al. determined the thermal resistance between a SWCNT and a solid sapphire substrate as 3 Km/W [36]. Recently, Carlborg et al. studied the thermal boundary resistance and the heat transfer mechanism between CNTs and an argon matrix using MD [37].

Recent molecular dynamics (MD) computations [34, 38] have found high values for tube–tube contact resistance. Maruyama et al. used MD simulations to compute the thermal boundary resistance between a CNT surrounded by six other CNTs using the lumped capacitance method [34]. By measuring the transient temperature change of CNTs they computed the CNT–CNT thermal resistance, and found it to be of the order of  $1.0 \times 10^{-7} \text{ m}^2\text{-K/W}$  [34]. Zhong and Lukes considered heat transfer between CNTs using classical MD simulations and estimated the interfacial thermal transport between offset parallel single-wall carbon CNTs as a function of CNT spacing, overlap, and length [38]. Greaney and Grossman used MD techniques to understand the effect of resonance on the mechanical energy transfer between CNTs [39]. It has been shown recently that the thermal resistance at a CNT–CNT contact should be of the order of  $0.3 \times 10^{-12} \text{ K/W}$  to match the very low conductivity measured for CNT beds. This has also been verified by atomistic Green's function (AGF) simulations [40]. Nevertheless, the mechanism of energy transport and phonon dynamics at the interface of two CNTs is still not well understood and needs a detailed exploration. Experimental techniques for direct measurement of CNT–CNT resistance have not yet been reported; thus atomistic-level simulations are a vital tool to analyze the interfacial transport mechanism.

In this article, we develop a systematic conceptual framework for understanding the electrical, thermal, and electro-thermal performance of CNT nanocomposites for macro-electronic applications. A generalized finite volume approach is presented for evaluating the electrical and thermal conductivity and device performance of nanotube network TFTs composed of finite two-dimensional nanocomposites. We first apply the approach to the prediction of the electrical and thermal conductance of pure percolating networks of CNTs in the absence of a substrate. Predictions of the electrical characteristics of pure-network TFTs in the linear regime are then presented and their behavior is explained by invoking the physics of heterogeneous finite-sized networks of metallic and semiconducting tubes. The numerical results for the estimation of the effective conductance properties of composites are presented next which explore the effect of tube-to-tube conductance, tube-to-substrate conductance and network density on both electrical and thermal transport. A two-dimensional effective medium

**Fig. 2** **a** Schematic of thin-film transistor showing source (S), drain (D) and channel (C). The channel region is composed of a network of CNTs. **b** Geometric parameters



approximation (EMA) is derived for thin-film composites and compared to our numerical simulations, and deficiencies in the EMA model for CNT composites are identified. Attention is turned next to the analysis of the thermal transport physics between two CNTs using molecular dynamics simulations and wavelet methods. We investigate the thermal interaction between two CNTs in a crossed configuration when a high temperature pulse is passed along one of the CNTs. Wavelet analysis decomposes the time series of the heat pulse in the time–frequency space and helps in determining the evolution and propagation of dominant modes.

## 2 Numerical Formulation

A schematic of a nanotube bundle transistor is shown in Fig. 1. In thin film structures, we often have three terminals—gate at the bottom, source and drain side by side, Fig. 2. TFTs are a special class of transistor in which a thin film of semiconducting material is used as the channel (C) region between the source and drain. In nanotube network TFTs, a thin CNT composite film acts as the channel region. Typical dimensions are indicated in Fig. 2b, where  $L_C$  is the length of the channel,  $L_t$  is the average length of the nanotubes,  $d$  is the diameter of nanotube,  $H$  is the width of the transistor and  $t$  is the thickness of the nanocomposite. A fixed voltage bias,  $V_{DS}$ , is applied across the channel from drain to source to drive the mobile charges in the channel region, while the transistor is turned on and off by

changing the gate voltage,  $V_{GS}$ . The corresponding current is denoted by  $I_{DS}$ . An important parameter to assess device performance is the on-off ratio ( $R$ ) which is the ratio of the current flowing in the device in the on-state,  $I_{ON}$ , to the current in device in the off-state,  $I_{OFF}$ .

In the present article, our analysis of the electrical performance of NNT TFTs is limited to the linear regime, a regime where current ( $I_{DS}$ ) through the device is linearly proportional to  $V_{DS}$ . This is only true at low  $V_{DS}$ . An extension of this problem has been reported by Pimparkar et al [41] that generalizes this problem to high-bias regime (high  $V_{DS}$ ) and provides proper scaling laws to predict the performance of transistors with arbitrary geometrical parameters and biasing conditions. For an insulating substrate (either for electrical or thermal transport), only transport in the percolating network of tubes is considered and the effective conductivity/conductance of the pure network is computed (see Sect. 3), Fig. 2a. If the substrate is sufficiently conducting, transport in both substrate and tube network are considered for computing effective conductive properties (see Sect. 4), incorporating the effect of tube-to-substrate interaction.

## 2.1 Thermal Transport

The computational domain for computing effective thermal properties of the nanotube composite is a three-dimensional box of size  $L_C \times H \times t$  (see Fig. 2b), which is composed of a 2D random network of nanotubes embedded in the mid-plane of the substrate. Diffusive transport in the tube obtains when there are a sufficient number of scattering events during the residence time of the phonon in the tube. This condition prevails here because of the dominance of interface scattering at the tube-substrate boundary. Thus, Fourier conduction in the nanotubes may be assumed, albeit with a thermal conductivity that may differ significantly from bulk or freestanding values. Assuming one-dimensional diffusive transport along the length  $s$  of the tube and three-dimensional conduction in the substrate, the governing energy equations [21] in the tube and substrate may be written in non-dimensional form as:

Tube:

$$\frac{d^2\theta_i}{ds^2} + \sum_{\text{intersecting tubes } j} Bi_c(\theta_j - \theta_i) + Bi_s(\theta_s - \theta_i) = 0, \quad (1a)$$

Substrate:

$$\nabla^2\theta_s + \sum_{i=1}^{N_{\text{tubes}}} Bi_s\beta_v \frac{k_t}{k_s}(\theta_i - \theta_s) = 0. \quad (1b)$$

Here, dimensionless temperature variable is  $\theta = (T - T_L)/(T_R - T_L)$ ;  $T_R$  and  $T_L$  are the face temperatures of the right and left boundary faces of the composite

(see Fig. 2b). These are the faces which contact source and drain when the thin film composite is used as the channel in the transistor. All lengths are non-dimensionalized by the tube diameter  $d$ .  $\theta_i (s^*)$  is the non-dimensional temperature of the  $i$ th tube at a location  $s^*$  along its length and  $\theta_s$  is the substrate temperature. The other dimensionless parameters are defined as:

$$Bi_c = \frac{h_c P_c d^2}{k_t A}; Bi_s = \frac{h_s P_s d^2}{k_t A}; \frac{k_s}{k_t}; \beta_v = \alpha_v \left( \frac{A}{P_s} \right); \frac{L_C}{L_t}; \frac{H}{L_t}; \frac{L_t}{d}; \frac{t}{d}$$

Here,  $Bi_c$  represents the dimensionless contact conductance for tube-to-tube contact;  $Bi_s$  represents the dimensionless interfacial conductance between the tube and substrate, both due to Kapitza resistance and isotherm distortion near the tube.  $A$  is the effective cross-section of the tube, and  $k_t$  is the corresponding thermal conductivity. The term  $h_c$  is the heat transfer coefficient governing the exchange of heat to other tubes  $j$  making contact with tube  $i$  through a contact perimeter  $P_c$ , and the heat transfer coefficient  $h_s$  governs the transfer of heat between the tube and the substrate through a contact perimeter  $P_s$ .  $k_s$  is the substrate thermal conductivity. The second term in Eq. (1b) contains the heat exchange with tubes traversing the substrate, which are  $N_{\text{tubes}}$  in number, through a contact area per unit volume,  $\alpha_v$ . The geometric parameter  $\beta_v$  may be determined from the tube density per unit area  $\rho$  and the corresponding dimensionless parameter is  $\rho^*$  ( $\rho/\rho_{th}$ ). The percolation threshold ( $\rho_{th}$ ) for the network is estimated as the density at which the average distance between the nanotubes equals the average length of the tubes, so that  $\rho_{th} = 1/1 \langle L_t \rangle^2$ .

For thermal conductivity calculations, the thermal boundary conditions for all tubes originating at the source and terminating in the drain are given by:

$$\theta_i = 1 \text{ at } s^* = 0; \theta_i = 0 \text{ at } s^* = \frac{L_t}{d}, \quad (2)$$

and the boundary conditions for the substrate are given by:

$$\theta_s = 1 \text{ at } x^* = 0; \theta_s = 0 \text{ at } x^* = \frac{L_C}{d}; \frac{\partial \theta_s}{\partial z^*} = 0 \text{ at } z^* = 0 \text{ and at } z^* = \frac{t}{d}. \quad (3)$$

All the tube tips terminating inside the substrate are assumed adiabatic. The boundaries  $y^* = 0$  and  $y^* = H/d$  are assumed as periodic boundaries for both substrate and tubes.

## 2.2 Electrical Transport

The dimensionless potential equation in the linear regime is analogous to the thermal transport equation in the Fourier conduction limit, with the potential being analogous to temperature and the current being analogous the heat transfer rate. For charge transport in CNTs in plastic, the substrate is considered insulating and



only transport in the tube network is considered. For organic transistors with dispersed CNTs [42], the substrate is not insulating and charge leaks from the CNTs to the organic matrix, analogous to thermal transport in a composite, and charge exchange with the substrate must be considered. Since  $L_C \gg \lambda$ , the mean free path of electrons, a drift–diffusion model and Kirchoff’s law for carrier transport may be employed [22]. In this linear regime, which occurs for low source-drain voltage  $V_{DS}$ , the current density along the tube is given by:

$$J = \sigma d\Phi/ds \quad (4)$$

where  $\sigma$  is the electrical conductivity and  $\Phi$  is the potential, and is only a function of the source-drain voltage  $V_{DS}$ . Using the current continuity equation  $dJ/ds = 0$  and accounting for charge transfer to intersecting tubes as well as to the substrate [43], the dimensionless potential distribution  $\phi_i$  along tube  $i$ , as well the three-dimensional potential field in the substrate are given by:

$$\frac{d^2 \phi_i}{ds^{*2}} + \sum_{\text{intersecting tubes } j} c_{ij}(\phi_j - \phi_i) + d_{is}(\phi_s - \phi_i) = 0, \quad (5a)$$

$$\nabla^{*2} \phi_s + \sum_{i=1}^{N_{\text{tubes}}} d_{is} \beta_v \frac{\sigma_t}{\sigma_s} (\phi_i - \phi_s) = 0. \quad (5b)$$

Here  $c_{ij}$  is the dimensionless charge-transfer coefficient between tubes  $i$  and  $j$  at their intersection point, analogous to  $Bi_c$  in Eq. (1a), and is specified a priori; it is non-zero only at the point of intersection. The term  $d_{is}$  is analogous to  $Bi_s$  term in Eq. (1a) and is active only for nanotubes in organic substrates. The electrical conductivity ratio is  $\sigma_t/\sigma_s$ . For computing the voltage distribution, boundary conditions  $\phi_i = 1$  and  $\phi_i = 0$  are applied to tube tips embedded in the source and drain regions respectively. For the organic substrate,  $\phi_s = 1$  and  $\phi_s = 0$  are applied at  $x^* = 0$  and  $x^* = L_C d$  respectively; for the other boundaries, a treatment similar to that for the substrate temperature is applied. This computation of voltage distribution is only valid for low  $V_{DS}$ .

### 2.3 Solution Methodology

In the present analysis, the nanotube network is essentially 2D, while the substrate containing it is 3D, as shown in Fig. 2b. The source, drain and channel regions in Fig. 2b are divided into finite rectangular control volumes. A fixed probability  $p$  of a control volume originating a nanotube is chosen a priori. A random number is picked from a uniform distribution and compared with  $p$ . If it is less than  $p$ , a nanotube is originated from the control volume. The length of source and drain for tube generation is  $L_t$ , which ensures that any tube that can penetrate the channel region from either the left or the right is included in the simulations. The orientation of the tube is

also chosen from a uniform random number generator. Since the tube length is fixed at  $L_t$ , all tubes may not span the channel region even for shorter channel lengths  $L_C$ , depending on orientation. Tubes crossing the  $y^* = 0$  and  $y^* = H/d$  boundaries are treated assuming translational periodicity; part of the tube crossing one of these boundaries reappears on the other side. Tube-tube intersections are computed from this numerically generated random network and stored for the future use. The analysis is conducted only on the tubes that lie in the channel region. The non-dimensional equations for the tubes and substrate are discretized using the finite volume method and a system of linearly coupled equations is obtained for the tube segment temperatures  $\theta_i$  (or the electric potential  $\phi_i$ ) and the substrate temperatures  $\theta_s$  (or the electric potential  $\phi_s$ ) at the substrate cell centroids. A direct sparse solver [44] is used to solve the resulting system of equations. To account for randomness in the sample, most of the results reported here are computed by taking an average over 100 random realizations of the network. More realizations are used for low densities and short channel lengths where statistical invariance is more difficult to obtain due to the small number of tubes in the domain.

### 3 Conduction in Percolating Network

If the underlying substrate (host matrix) has very low conductivity, the network itself forms the dominant pathway for conduction. This limit is realized in the case of electrical conduction in nanotube composites when the network is embedded inside an almost-insulating substrate such as plastic or glass. For thermal conduction in nanotube composites, the substrate-to-tube conductivity ratio is generally higher than for electrical conduction and substrate-to-tube interaction can be neglected only when the interfacial resistance between the tube and substrate is extremely high [21]. Therefore, the pure network conduction case is generally not realized for thermal transport.

The conductive properties of the network are strongly dependent on the density of the tubes in the network. A conducting path between source and drain may not exist at very low tube densities. If such tube network is used as the channel region of the transistor, no current could pass through the transistor. As the density of tubes increases, a critical density  $\rho_{th}$ , known as the percolation threshold, is reached, at which a complete pathway between source and drain is formed. The percolation threshold for the network is estimated as the density at which the average distance between the nanotubes equals the average length of the tubes, so that  $\rho_{th} \propto 1/\langle L_t \rangle^2$ . A more accurate dependence of  $\rho_{th}$  on tube length, given by  $\rho_{th} = 4.23^2/\pi L_t^2$ , can be obtained from the numerical simulations [45, 46]. There is great interest in exploring the transport behavior of the network at densities close to the threshold, which is dependent on the dimensionality and the aspect ratio of the tubes. Close to the percolation threshold, the network conductance,  $G$ , exhibits a power-law relation, i.e.  $G \sim (\rho - \rho_{th})^m$ , where  $m$  is the percolation exponent [47].

Several studies based on the Monte-Carlo simulations have been reported for the analysis of the percolating networks of nanotubes or their composites [31, 47]. Keblinski and Cleri [31] analyzed the effect of contact resistance in percolation networks to explain why the value of the percolation threshold scaling exponent holds over the entire range of network-densities. Foygel et al. [47] performed Monte Carlo simulations to explore the aspect ratio dependence of the critical fractional volume and the critical index of conductivity. Shenogina et al [48] performed finite element analysis to explore the reasons for the absence of thermal percolation in nanotube composites. We have performed a percolation-based analysis to compute the conductance exponents of nanotube networks for different densities and for different tube-to-tube contact conductances [13]. We have also explored the change in the device performance when the semi-conducting tube network in the channel region is contaminated by metallic tubes [22]. Important results from these studies are summarized below.

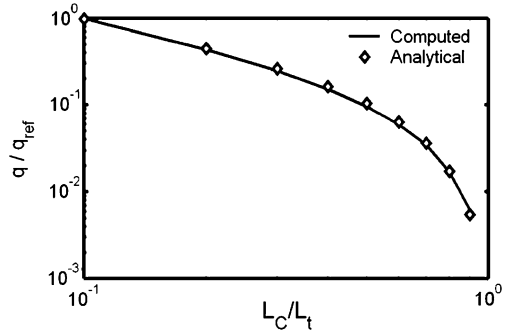
### 3.1 Network Transport in the Non-Contacting Limit

In the limit when there is no contact between tubes ( $Bi_c = 0$ ,  $c_{ij} = 0$ ) and between tube and substrate ( $Bi_s = 0$ ,  $d_{is} = 0$ ) and tubes directly bridge source-drain, a simple analytical solution for the heat transfer rate through the domain (and correspondingly the drain current  $I_{DS}$  for electron transport) may be derived. Only the tubes are considered in this 2D planar calculation, and the substrate contribution is neglected. In this limit, the in-plane heat transfer rate through the composite,  $q$ , is directly proportional to the number of tubes directly bridging source and drain, but inversely proportional to the tube length contained in the channel. By computing the number of bridging tubes from geometric considerations, it may be shown that [13]:

$$q \propto I_{DS} \propto \frac{N_S}{W} = \left(\frac{2}{\pi}\right) \rho H L_t \left( \cos^{-1} \left( \frac{L_C}{L_t} \right) - \left( \frac{L_C}{L_t} \right) \sqrt{1 - \left( \frac{L_C}{L_t} \right)^2} \right). \quad (6)$$

where  $W$  is  $\left[ \sum_{i=1}^{N_S} 1/L_i \right]^{-1}$ ,  $L_C$  is the channel length shown in Fig. 2,  $L_t$  is the length of the tube, and  $H$  is the height of the sample, as shown in Fig. 2,  $N_S$  is number of bridging tubes and  $\rho$  is the density of the tubes. The constant of proportionality in Eq. (6) depends on the conductivity of the tubes. Figure 3 shows a comparison of the analytical result obtained using Eq. (6) with that computed numerically using the finite volume method described above. The ratio  $q/q_{ref}$  is plotted, where  $q_{ref}$  is the reference heat transfer rate at  $L_C/L_t = 0.1$ . One hundred random realization of the network are used. The case  $L_C = 3 \mu\text{m}$ ,  $H = 4 \mu\text{m}$ , and  $\rho = 5.0 \mu\text{m}^{-2}$  is considered. The analytical and numerical results are in good agreement with each other, confirming the validity of our approach. When the

**Fig. 3** Comparison of heat transfer rate in a nanotube network with analytical results for the case of zero tube–tube contact



channel length becomes comparable to or longer than the tube length,  $q/q_{ref}$  is seen to go to zero; in the absence of tube–tube and tube–substrate contact, heat or current can flow through the tubes only if the tubes bridge source and drain. As a practical matter, the result in Fig. 3 is applicable to electrical transport in short-channel CNT/plastic TFTs where the short channel lengths imply few tube–tube interactions.

### 3.2 Conduction Exponents

The lateral electrical conductivity of CNT thin films has been measured by different research groups. Here, we compare the network conductance predicted using our model with electrical conductance measurements by Snow et al. [10]. A pure planar tube network is considered, assuming that the substrate is entirely non-conducting. This is typical of electrical transport in CNT/plastic composites. The average length of the tubes in Reference [10] ranges from 1 to 3  $\mu\text{m}$ . The exact length distribution of nanotubes has not been reported in Snow et al. [10]. For the numerical model, random networks with a tube length of 2  $\mu\text{m}$  are generated, and an average over 200 random realizations is taken. The percolation threshold for the network is roughly estimated using  $\rho_{th} = 1/1\langle L_t \rangle^2$  to be 0.25  $\mu\text{m}^{-2}$ . Simulations are performed for densities in the range 1–10  $\mu\text{m}^{-2}$  for channel lengths varying from 1 to 25  $\mu\text{m}$  and with a width  $H$  of 90  $\mu\text{m}$ , corresponding to the dimensionless parameters  $L_C/L_t \sim 0.5\text{--}12.5$  and  $H/L_t = 45$ . The device dimensions and tube lengths are chosen to match those in Reference [10].

In Fig. 4a, the normalized network conductance  $G/G_0$  is shown as a function of  $L_C/L_t$  for several tube densities above the percolation threshold for nearly perfect tube–tube contact (i.e.,  $c_{ij} = 50$ ). For long channels ( $L_C > L_t$ ) there are no tubes directly bridging the source and drain, and current (heat) can flow only because of the presence of the network. If the tube density is greater than the percolation threshold, a continuous path for carrier transport exists from source to drain, and  $G$  is seen to be non-zero even for  $L_C/L_t > 1$ . Figure 4a shows that the conductance exponent,  $n$ , defined as  $G \sim (L_C)^n$ , is close to  $-1.0$  for the high densities

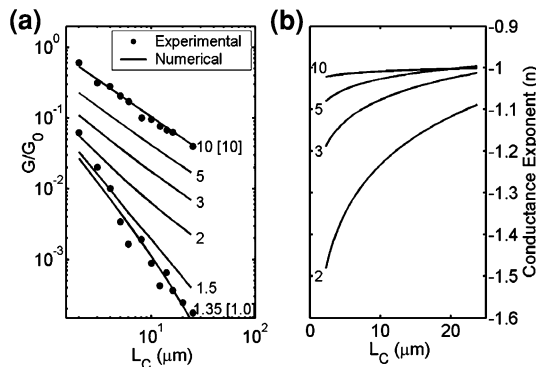


**Fig. 4** **a** Computed conductance dependence on channel length for different densities ( $\rho$ ) in the strong coupling limit ( $c_{ij} = 50$ ) compared with experimental results from Ref. [11]. For  $\rho = 10.0 \mu\text{m}^{-2}$ ,  $G_o = 1.0$  (simulation),  $G_o = 1.0$  (experiment). For  $\rho = 1.35 \mu\text{m}^{-2}$ ,  $G_o = 1.0$  (simulation),  $G_o = 2.50$  (experiment). The number after each curve corresponds to the value of  $\rho$  used in the simulation. The number in [ ] corresponds to  $\rho$  in experiments from Ref. [11]. **b** Dependence of conductance exponent ( $n$ ) on channel length for different densities ( $\rho$ ) based on Fig. 4a

( $\rho = 10 \mu\text{m}^{-2}$ ;  $\rho^* = \rho/\rho_{th} = 40$ ), indicating ohmic conduction, in good agreement with Snow et al. [11]. The exponent increases to  $-1.80$  at lower densities ( $1.35 \mu\text{m}^{-2}$ ;  $\rho^* = 5$ ), indicating a non-linear dependence of conductance on channel length. The asymptotic limit of the conductance exponent for infinite samples with perfect tube/tube contact has been found to be  $-1.97$  [49, 51]. The observed non-linear behavior for low density is expected because the density value is close to the percolation threshold. Snow et al. reported a conductance-exponent of  $-1.80$  for a density of  $1.0 \mu\text{m}^{-2}$  and channel length  $>5 \mu\text{m}$ . For the same device dimensions, this value of the exponent is close to that obtained from our simulations for a density of  $1.35 \mu\text{m}^{-2}$ . At densities close to the percolation threshold, computations are very sensitive to variations in computational parameters. Small variations in experimental parameters such as tube diameter, nanotube contact strength, tube electronic properties as well as the presence of a distribution of tube lengths ( $1-3 \mu\text{m}$ ), which is not included in the simulation, may explain the difference. The contact resistance between the nanotubes and the source and drain electrodes as well as insufficiently large samples for ensemble averaging in the experimental setup may also be responsible. Indeed, a more quantitative agreement with the low-density data at short channel length is realized if one accounts for imperfect tube-tube contacts [51].

The dependence of conductance exponent on channel length is explored in Fig. 4b for  $c_{ij} = 50$  and for densities in the range  $2.0-10 \mu\text{m}^{-2}$ , corresponding to  $\rho^*$  values of  $8-40$ . For densities  $>3.0 \mu\text{m}^{-2}$  ( $\rho^* > 12$ ), the exponent approaches the ohmic limit,  $-1.0$ , with increasing channel length. Larger exponents, corresponding to non-ohmic transport, are observed for the shorter channel lengths. This is consistent with experimental observations, where conductance is seen to scale more rapidly with channel length for small  $L_C$  [11].

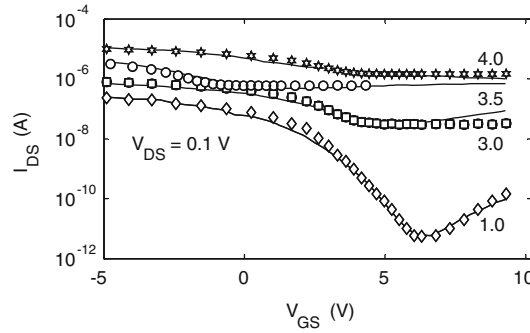


**Fig. 5** Computed  $I_{DS} \sim V_{GS}$  at  $V_{DS} = 0.1$  V for different densities is compared with experimental results from Ref. [11] before the electrical breakdown of metallic tubes. Solid lines correspond to experimental results from Ref. [11] and markers correspond to computational results. The number after each curve corresponds to tube density  $\rho$ . The curve  $\rho = 3.5 \mu\text{m}^{-2}$  is shifted on the x-axis to account for charge trapping

### 3.3 Conduction in Heterogeneous Networks of Metal-Semiconducting Tubes

The electrical performance of CNT networks is strongly influenced by the fact that approximately one-third of the CNTs grown by typical processing techniques exhibit metallic behavior and approximately two-third exhibit semiconducting behavior [22]. This heterogeneity controls the on-off ratio  $R$  of typical CNT-network based devices, where on-off ratio  $R$  is the ratio of the device-current in the on state to the device current in the off-state.  $R$  has been shown [22] to be a unique and predictable function of  $L_C$ ,  $L_b$ ,  $N_{IT}$  (the density of interface traps),  $f_M$  (the degree of metallic contamination) and  $\rho$ , the tube density. In the conventional transistors,  $N_{IT}$  is the trapped charge at the interface of the channel and the insulating dielectric  $\text{SiO}_2$ , which separates the gate from the channel.  $f_M$  is the ratio of the number of metallic tubes to semi-conducting tubes in the tube-network. If the on-off ratio  $R$  can be reliably predicted as a function of tube density  $\rho$  and other parameters, our numerical model affords a unique way to find the tube density of typical CNT thin films by using this relationship in the inverse. This method promises far more accurate estimation of ‘electrically relevant’ tube density than methods currently in use, such as atomic force microscopy, and scanning electron microscopy [11].

We compute  $I_{DS}$  versus  $V_{GS}$  for several tube densities ( $\rho = 1\text{--}5 \mu\text{m}^{-2}$ ) for device parameters  $L_C = 10 \mu\text{m}$ ,  $L = 2 \mu\text{m}$ ,  $H = 35 \mu\text{m}$ , and  $V_{DS} = 0.1$  V, (Fig. 5) which are chosen to match the experiments in [10]. Since  $L_C \gg L_b$ , these transistors are called long-channel devices (note that this terminology differs from classical transistor terminology—where long and short channels are defined with respect to electrostatic control of the channel by the gate electrode [52]). We use  $c_{ij}$

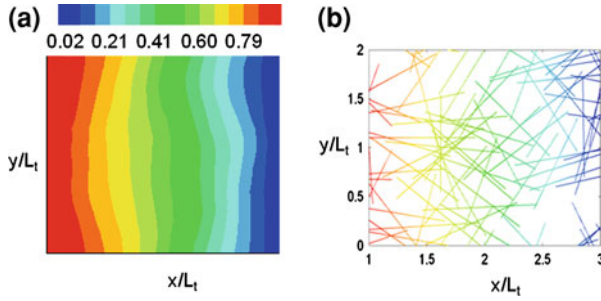


**Fig. 6** Non-dimensional temperature distribution in **a** substrate **b** tube network.  $L_c/L_t = 2.0$ ,  $H/L_t = 2$ ,  $Bi_c = 10.0$ ,  $Bi_s = 10^{-5}$ ,  $k_s/k_t = 0.001$  and  $\rho^* = 14.0$

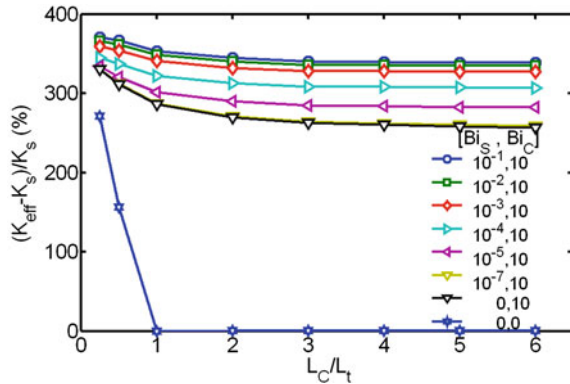
$\sim 50$  based on typical values for CNT tube–tube contact [11, 53], mobility [11] and density functional theory. Here,  $f_M$ , is taken to be 33% in Fig. 5, consistent with Snow et al. [11]. The conductance ratio of metallic to semiconducting tubes (M/S conductance ratio) in the on-state is chosen as 8.0, consistent with Reference [54]. In general, the M/S conductance ratio depends weakly on the fabrication process, as well as the chirality, band-gap and the diameter of the tubes.

Gate characteristics, represented by  $I_{DS}-V_{GS}$  curves, are computed for a specific network configuration. An average is then taken over 50 random realizations of the network. Computations for  $\rho = 1 \mu\text{m}^{-2}$  agree very well with experiments in Ref. [11], Fig. 5. Increasing  $\rho$  increases the number of percolating metallic paths, increasing the on-current  $I_{ON}$ , but reducing  $R$ , as in Ref. [10]. Snow et al. speculate that  $\rho > 3 \mu\text{m}^{-2}$  for devices with low on–off ratio (top three solid lines in Fig. 5). Our simulations establish that they correspond to exact densities of  $\rho = 3.0$ , 3.5 and 4.0 respectively. Thus, tube density  $\rho$  may be deduced from a simple electrical measurement of the on/off current ratio (see Fig. 5) obviating the need for inaccurate and time-consuming analysis of AFM images, as is currently done. We note, however, that although we can predict  $R(\rho)$  for a fixed M/S conductance ratio and  $c_{ij}$ , the absolute value of the on–off current and  $R$  can still vary from sample to sample depending on the M/S conductance ratio and the contact conductance between tubes of different diameters. The same methodology can also be used to interpret short channel data (Fig. 2 in Ref. [8], for example). This demonstrates the predictive power of the theoretical framework.

## 4 Conduction in Nanotube: Polymer Composites

Thus far, we have considered conduction in a pure network of nanotubes in the absence of a substrate or host matrix. We now turn our attention to thermal and electrical conduction in composites where carrier transport is no longer confined exclusively to nanotube network. When the thermal conductivity ratio  $k_s/k_t$  is

**Fig. 7** Effect of substrate-tube contact conductance ( $Bi_S$ ) on  $k_{eff}$  for varying channel length.  $L_C/L_t = 0.25-6.0$  ( $L_t = 2.0 \mu\text{m}$ ),  $H/L_t = 2$ ,  $k_s/k_t = 0.001$ , and  $\rho^* = 3.5$  ( $\rho = 5.0 \mu\text{m}^{-2}$ )



significant or when the heat leakage from the tubes to the substrate is significant, both substrate and network play important roles in determining the thermal performance of typical nanotube composites. For electrical transport, the substrate does not generally play a role in nanotube-polymer composites, since the polymer is essentially insulating. However, a problem analogous to thermal transport occurs in electrical transport in nanotube-organic composites. Here, the electrical conductivity of the organic substrate is relatively large, and forms the primary conduction pathway. Recently, sub-percolating nanotube dispersions have been added to enhance electrical conductivity of organics [42].

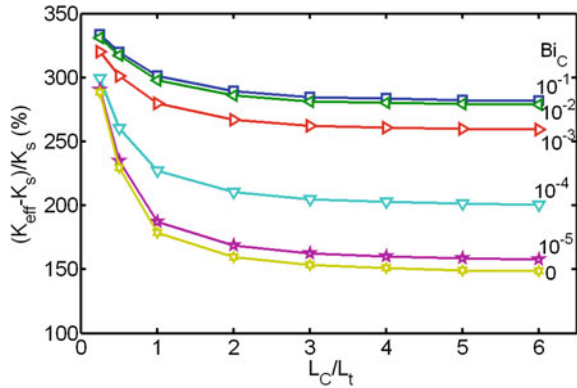
Using the formulation described in Sect. 3, a typical temperature distribution in the tube network and the substrate is computed and shown in Figs. 6a, b. For this case,  $L_C/L_t = 2.0$ ,  $H/L_t = 2$ ,  $Bi_C = 10.0$ ,  $Bi_S = 10^{-5}$ ,  $k_s/k_t = 0.001$  and  $\rho^* = 14.0$ , corresponding to  $L_C = 4 \mu\text{m}$ ,  $L_t = 2 \mu\text{m}$ ,  $H = 4 \mu\text{m}$ , and  $\rho = 3.5 \mu\text{m}^{-2}$ . Contours of constant temperature in the substrate would be one-dimensional in  $x$  for  $Bi_S = 0$ , but due to the interaction with the tubes, distortion in the contours is observed, consistent with the temperature plots in the tube in Fig. 6b. The departure from one-dimensionality in the substrate temperature profile is related to local variations in tube density; regions of high tube density convey the boundary temperature further into the interior.

#### 4.1 Effect of Tube-Substrate Interfacial Resistance

The contact parameters  $Bi_S$  for tube-substrate contact and  $Bi_C$  for tube-tube contact are difficult to determine, and there are few guidelines in the literature to choose them. The experimental studies conducted by Huxtable et al. [55] suggest that heat transport in nanotube composites may be limited by exceptionally small interfacial thermal conductance values. The value of the interfacial resistance between the carbon nanotube and the substrate was reported to be  $8.3 \times 10^{-8} \text{ m}^2 \text{ K/W}$  by Huxtable et al. [55] for carbon nanotubes in hydrocarbon (do-decyl



**Fig. 8** Effect of tube–tube contact conductance ( $Bi_C$ ) on  $k_{eff}$  for varying channel length.  $L_C/L_t = 0.25–6.0$  ( $L_t = 2.0 \mu\text{m}$ ),  $H/L_t = 2$ ,  $k_S/k_t = 0.001$ ,  $Bi_S = 10^{-5}$ , and  $\rho^* = 3.5$  ( $\rho = 5.0 \mu\text{m}^{-2}$ )

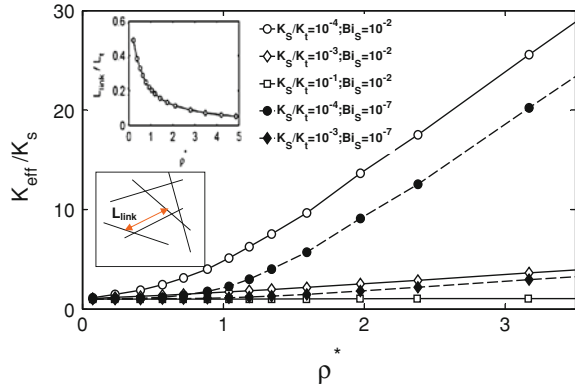


sulphate). The non-dimensional contact parameter  $Bi_S$  evaluated using this contact conductance is  $O(10^{-5})$  assuming the thermal conductivity of a single SWCNT to be 3,000 W/mK. The corresponding values for nanotube-polymer or nanotube-glass interfaces are not known at present. Consequently, values of  $Bi_S$  in the range  $10^{-1}–10^{-7}$  were considered. If we assume the thermal conductivity of the polymer matrix to be 0.25 W/mK, a value of  $Bi_S = 10^{-5}$  corresponds to the thermal resistance of an equivalent polymer layer of thickness 20 nm.

The percentage increase in  $k_{eff}$  of the composite is plotted against  $L_C/L_t$  ratio for different  $Bi_S$  in Fig. 7 for,  $L_C/L_t \sim 0.25–6.0$  ( $L_t = 2.0 \mu\text{m}$ ),  $H/L_t = 2$ ,  $k_S/k_t = 0.001$ , and  $\rho^* = 3.5$  ( $\rho = 5.0 \mu\text{m}^{-2}$ ). Here, the tube density is much higher than the percolation threshold density,  $\rho_{th} \sim 1.42 \mu\text{m}^{-2}$ . The tube–tube contact parameter is held at  $Bi_C = 10$ , denoting nearly perfect contact. The conductivity ratio is  $10^{-3}$ , denoting highly conducting tubes in a relatively insulating substrate. A sharp increase in  $k_{eff}$  is observed for shorter channel lengths as a result of highly conducting tubes directly bridging source and drain. This increase for shorter channel lengths is less significant at high  $Bi_S$  due to high heat leakage from the tubes to the substrate. As the channel length increases, the composite approaches bulk behavior and the conductance achieves invariance beyond  $L_C/L_t > 5$ . The asymptotic values of  $k_{eff}$  at high channel lengths ( $L_C/L_t > 5$ ) can be expressed as  $k_{eff} \sim 1 + \gamma k_S/k_t$ , where  $\gamma$  is dependent on  $Bi_S$ ,  $Bi_C$  and area-ratio of tubes cross-section and substrate at a composite cross-section. The general shape of the curves is explained by the ‘zero  $Bi_S$ , zero  $Bi_C$ ’ case. As the channel becomes narrower, bridging occurs and so the curve rises. This is a “finite-size” effect not seen in bulk composites, and exists even for channels 3–4 times the tube length.

It is observed that the curve for  $Bi_S \sim 10^{-7}$  is the same as that for  $Bi_S \sim 0$ , Fig. 7. This defines the lower limits of tube-substrate contact—below this only the network is active and side-leakage disappears. For this case, the only reason for the existence of a non-zero  $k_{eff}$  increase is the network. In this limit we expect percolation behavior, unlike that noted in the literature [27]. This implies that the interface resistance is far smaller than that corresponding to  $Bi_S = 10^{-7}$  in Biercuk et al. [27]. The tube-substrate contact parameter  $Bi_S$  ceases to be limiting for  $Bi_S >$

**Fig. 9** Variation of normalized effective thermal conductivity ( $k_{eff}/k_S$ ) against normalized tube density ( $\rho^* = \rho/\rho_{th}$ ) is shown for different  $k_S/k_t$  and  $Bi_S$ . Average link-length ( $L_{link}$ ) dependence on  $\rho$  is shown in the inset. A typical link length is shown in the bottom inset.  $L_C/L_t = 3$  ( $L_t = 2.0 \mu\text{m}$ ),  $H/L_t = 2$ ,  $Bi_C = 10$



$10^{-2}$ , and the  $k_{eff}$  variation with  $L_C/L_t$  becomes independent of  $Bi_S$  beyond this value.

The network causes a 150–350% increase in  $k_{eff}$  over the substrate, but this still means values only in the 0.35–3.5 W/mK, implying that the composites does not conduct very well laterally, despite the presence of highly conducting tubes. Since the  $k_S/k_t$  value used here is expected to be typical of many composites for TFT applications, the results in this section demonstrate that if the percolation properties of the network could be maintained by high tube–tube contact conductance, the network itself could provide a pathway for heat removal.

## 4.2 Effect of Tube–Tube Conductance

Recently, Lukes et al. [38] considered heat transfer between CNTs using classical molecular dynamics simulations, and estimated a tube–tube contact resistance of the order of  $1.0 \times 10^{-7} \text{ m}^2\text{-K/W}$ , corresponding to a  $Bi_C$  value of  $2.0 \times 10^{-5}$  (assuming  $k_t = 3,000 \text{ W/mK}$ ). However, there is no experimental corroboration of tube–tube contact resistance, and  $Bi_C$  values of  $0$ – $10^{-1}$  are chosen, ranging from insulating contact to perfect contact. Previous theoretical models for computing  $k_{eff}$  of nanotube composites ignore contact conductance between the nanotubes [26]. Since tube–tube contact occurs over a very small contact area, this contact resistance would be limiting only in the case of large tube-substrate resistance ( $Bi_S \rightarrow 0$ ) for most  $k_S/k_t$  values of interest. Figure 8 show the  $k_{eff} \sim L_C/L_t$  plots for different  $Bi_C$  for  $L_C/L_t \sim 0.25$ – $6.0$  ( $L_t = 2.0 \mu\text{m}$ ),  $H/L_t = 2.0$ ,  $k_S/k_t = 0.001$ ,  $Bi_S = 10^{-5}$ , and  $\rho^* = 3.5$  ( $\rho = 5.0 \mu\text{m}^{-2}$ ). The overall shape of the curves is similar to that in Fig. 7. The sharp increase in  $k_{eff}$  for shorter channel length composites (due to bridging tubes) is significant for low  $Bi_C$ , but the effect gradually diminishes with increasing  $Bi_C$ , Fig. 8. Decreasing  $Bi_C$  from  $10^{-1}$  to  $10^{-5}$  decreases  $k_{eff}$  by about 50% for long channels. Beyond  $Bi_C > 10^{-2}$ , tube–tube contact is sufficiently good that it ceases to matter; consequently the  $k_{eff}$  curves become coincident in

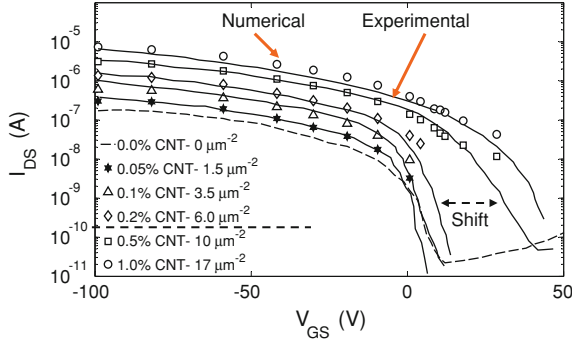


**Fig. 10** Computed  $I_{DS}-V_{GS}$  at  $V_{DS} = -10$  V for different CNT-densities ( $\rho \sim 1-17 \mu\text{m}^{-2}$ ) is compared with experimental results in [42]. The volume percentage of CNT dispersions used in the experiments and the corresponding network density ( $\rho \mu\text{m}^{-2}$ ) used in the computations are shown.  $L_t = 1 \mu\text{m}$ ,  $L_C = 20 \mu\text{m}$  and  $H = 200 \mu\text{m}$ . The shift in the  $I_{DS}-V_{GS}$  curves due to the initiation of semiconducting CNT percolation for CNT volume percentage  $>0.2\%$  is shown by the dashed arrow

Fig. 8. By the same token, values of  $Bi_C$  below  $10^{-5}$  mean essentially zero contact between tubes, and heat leakage through the substrate is the only pathway for heat transfer for long channels. The tube-tube contact resistance computations by Zhong and Lukes [38] suggest that this may indeed be the mechanism of heat transfer in CNT composites, though further experimental corroboration is necessary. The present analysis reveals that for tube densities higher than the percolation threshold,  $Bi_C$  may be an important parameter controlling  $k_{eff}$  for highly conducting tubes with high tube-substrate resistance.  $Bi_C$  ( $10^{-2}-10^{-5}$ ) corresponds to the thermal resistance presented by an equivalent polymer matrix of thickness 0.025–25 nm assuming contact area between the tubes of the order  $\sim d^2$  and  $k_S/k_t = 10^{-3}$ .

### 4.3 Effect of Tube Density

The effective thermal conductivity of the composite is observed to have a different dependence on  $\rho$  in different regimes, i.e.  $\rho \ll \rho_{th}$ ,  $\rho \sim \rho_{th}$  and  $\rho \gg \rho_{th}$  [56].  $k_{eff}$  is shown as a function of  $\rho$  for these three different regimes in Fig. 9 for the case  $\rho_{th} (= 4.23^2/\pi L_t^2 \sim 1.4 \mu\text{m}^{-2})$ ,  $k_S/k_t \sim 10^{-4} - 10^{-1}$ ,  $Bi_S \sim 10^{-7} - 10^{-2}$ ,  $L_C/L_t = 3$  ( $L_t = 2.0 \mu\text{m}$ ),  $H/L_t = 2$ ,  $Bi_C = 10$ . When  $\rho \ll \rho_{th}$ ,  $k_{eff}$  increases linearly with  $\rho$ . This is expected since the tubes do not interact with each other either through direct contact or through the substrate. This lack of tube-tube interaction is borne out by the variation of the average link length ( $L_{link}$ ) with  $\rho^*$  (inset in Fig. 9), which shows that the non-interacting limit between tubes is achieved for  $\rho^* \ll 1$  for which  $L_{link}/L_t \sim 1$ . This trend is in agreement with the results from EMA which predict a linear scaling with volume fraction. When  $\rho \sim \rho_{th}$ ,  $k_{eff}$  is observed

to vary non-linearly with  $\rho$ . This is typical of network percolation close to the percolation threshold [11, 13] and becomes more pronounced with decreasing  $Bi_S$  or  $k_S/k_t$ , Fig. 9. These two parameters explain the difference between percolation behavior for thermal transport and for electrical transport. Strong non-linear behavior near the percolation threshold is observed for charge transport in CNT-polymer composites due to very low  $k_S/k_t$  ( $<10^{-6}$ ) [11, 13], while for thermal transport, this non-linear behavior is relatively weak due to high  $k_S/k_t$  ( $\sim 10^{-3}$ ) and high heat leakage through the substrate (high  $Bi_S$ ). Whenever transport through the substrate competes with the transport through the CNT network either due to high  $k_S$  or due to high heat leakage from the CNTs to the substrate, percolation effects due to the network are suppressed.

For  $\rho > 3.0\rho_{th}$  and for large enough  $L_C/L_t$ ,  $k_{eff}$  is found to vary linearly with  $\rho$ , Fig. 9. The reason for this is evident in the inset in Fig. 9, which shows that the average  $L_{link}$  varies linearly with  $\rho^*$  for high densities ( $\rho^* > 3$ ). Hence the network becomes homogenous. Computations of  $k_{eff}$  for the pure network in the absence of the substrate [13] reveal that it may be expressed as  $k_{eff}/k_t \sim \rho L_t^2 (0.783 - 0.119 \ln(Bi_C^2) - 0.015 \ln(Bi_C))$  for high densities. For the CNT composites, this expression would also depend on  $Bi_S$  and  $k_S/k_t$ , but linearity with respect to density would nevertheless be valid.

#### 4.4 Electrical Conductivity of CNT-Organic Composites

A novel approach involving modifying the transconductance ( $g_m \sim dI_{DS}/dV_{GS}$ ) of an organic host using a sub-percolating dispersion of CNTs has been proposed in Ref. [42]. A 60-fold decrease in effective channel length,  $L_{eff}$ , is observed that results in a similar increase in  $g_m$  with a negligible change in on-off ratio [42]. In this technique, the majority of the current paths are formed by the network of CNTs, but short switchable semiconducting links are required to complete the channel path from source to drain [42]. Experimental data published in Ref. [42] provide a good opportunity to test the correctness of our numerical formulation in Sect. 3.

The device parameters  $L_C = 20 \mu\text{m}$ ,  $L_t = 1 \mu\text{m}$ , and  $V_{DS} = -10 \text{ V}$  are chosen to match the experiments in Ref. [42]. Charge transfer coefficients  $c_{ij} = 10^{-4}$  and  $d_{is} = 10^{-4}$  are assumed and correspond to poor contact conductance between tube-tube and tube-substrate. The electrical conductivity ratio,  $\sigma_t/\sigma_s$ , for metallic CNTs in the on-state ( $V_{GS} = -100 \text{ V}$ ) is taken as  $5.0 \times 10^4$ , while that for semiconducting CNTs is  $5.0 \times 10^3$  [54]. The metallic-CNT conductivity is assumed constant with  $V_{GS}$ , while the roll-off in the conductivity of semiconducting CNTs and the organic-matrix with  $V_{GS}$  is obtained from the experimental  $I_{DS}$ - $V_{GS}$  curves (0 and 0.5% volume fraction curves) in Fig. 14.1b of Ref. [42]. Figure 10 shows that numerical results agree well with experiments over the entire range of tube densities ( $1.5$ – $17 \mu\text{m}^{-2}$ ). There is an anomalous jump in the  $I_{DS}$ - $V_{GS}$  curve for 0.5% volume fraction of CNTs (labeled “shift” in Fig. 10; see also

**Fig. 11 a** Comparison of normalized effective thermal conductivity ( $k_{eff}/k_S$ ) computed from numerical simulations (markers) and analytically-derived expressions (*solid lines*) for different  $k_S/k_t$  ratios.  $L_C/L_t = 8$  ( $L_t = 0.5 \mu\text{m}$ ),  $H/L_t = 4$ ,  $Bi_S = 10^{-5}$  and  $\rho^* = 0-0.3$  ( $\rho = 0.1-6.5 \mu\text{m}^{-2}$ ).  $Bi_C = 0$  for simulations unless otherwise stated. **b** Comparison of normalized effective thermal conductivity ( $k_{eff}/k_S$ ) computed from numerical simulations and 2D EMA for different values of the interfacial thermal resistance  $Bi_S$  ( $10^{-7}-10^{-5}$ ).  $L_C/L_t = 8$  ( $L_t = 0.5 \mu\text{m}$ ),  $H/L_t = 4$ ,  $k_S/k_t = 10^{-3}$  and  $\rho^* = 0-0.3$  ( $\rho = 0.1-6.5 \mu\text{m}^{-2}$ )

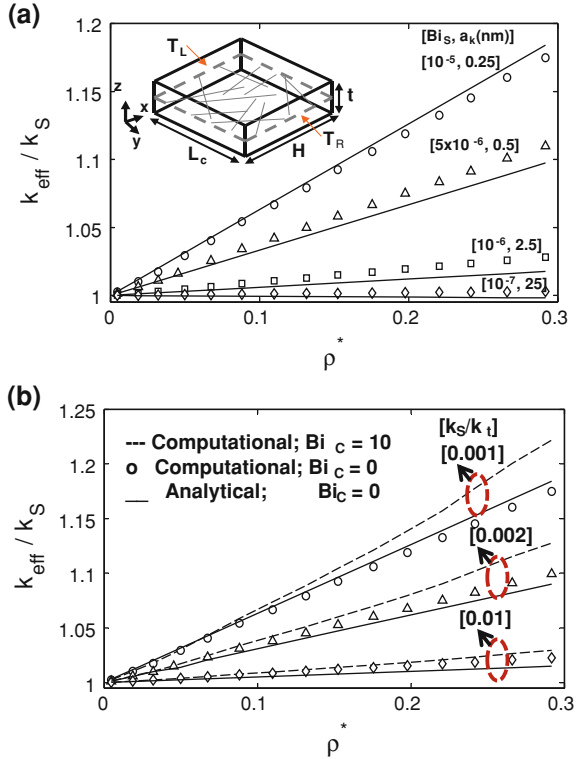
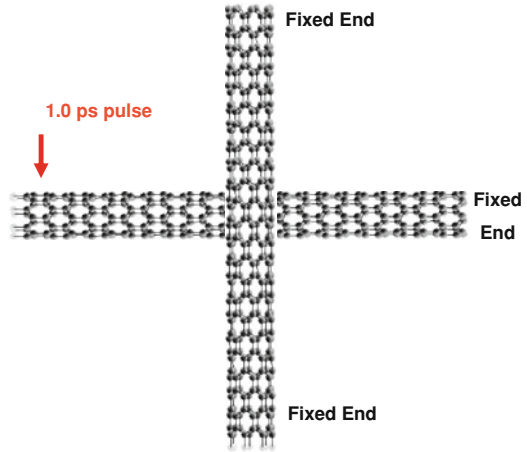


Fig. 14.1b in Ref. [42]) which is not properly understood. We calculated the  $I_{DS}-V_{GS}$  characteristics of the organic TFT device in [42] with a realistic heterogeneous network of semiconducting-metallic tubes (1:2 ratio) dispersed in an organic matrix. We have shown that this anomalous shift in the  $I_{DS}-V_{GS}$  curve is a consequence of the formation of a parallel sub-percolating network of *semiconducting* CNTs in the organic matrix. At 0.2% CNT volume fraction, the semiconducting tubes do not have sufficient density to form a percolating network in and of themselves; metallic CNTs are necessary to achieve percolation. However, when the volume fraction is increased to 0.5%, semiconducting tubes can form a percolating network by themselves, and shift the  $I_{DS}-V_{GS}$  curve as shown. This confirms that semiconducting CNTs are active elements of this organic TFT device, a feature which was not understood previously.

### 4.5 Comparison with Effective Medium Theory

For low-density dispersions, the effective conductivity ( $k_{eff}$ ) can be derived using a Maxwell-Garnett effective medium approximation [18], and provides a baseline

**Fig. 12** Schematic of two CNTs in a crossed configuration. A 1.0 ps pulse is generated from one end of the first tube, while atoms at the other end are kept fixed. The two ends of the other tube are kept fixed. The chiralities of the two tubes are the same



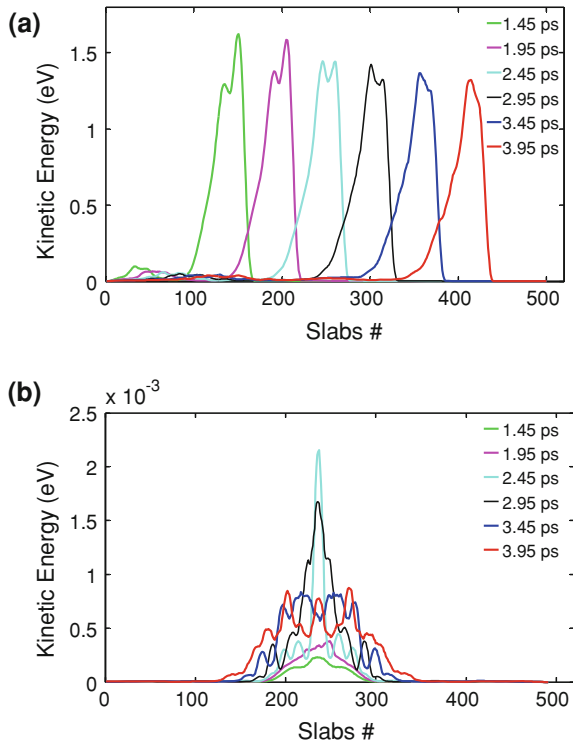
for comparison with our numerical calculations. For a planar CNT network isotropic in the x–y plane (see inset in Fig. 11b) and embedded in a substrate of thickness  $d$ , the theory in [18] may be modified to yield  $k_{eff}$  in the x–y plane as

$$k_x = k_y = k_S \frac{2 + f[\beta_{11}(1 - L_{11}) + \beta_{33}(1 - L_{33})]}{2 - f[\beta_{11}L_{11} + \beta_{33}L_{33}]} \quad (7)$$

Here  $f$  is the volume fraction,  $L_{ii}$  is the depolarization factor, and  $\beta_{ii} = \frac{k_{ii} - k_S}{k_S + (k_{ii} - k_S)}$ ;  $k_{11} = k_{22} = \frac{k_t}{1 + (2a_K k_t / k_S d)}$ ;  $k_{33} = \frac{k_t}{1 + (2a_K k_t / k_S L_t)}$ . Here,  $a_K$  is the Kapitza radius [18, 26], axis 3 represents the longitudinal axis of the CNT and axes 1 and 2 are the other two axes of the CNT [18].

The finite volume computation of  $k_{eff}$  is compared with predictions from the 2D EMA in Figs. 11a, b [56]. For this case, the polarization factors are given by  $L_{11} = L_{22} = 0.5$ ,  $L_{33} = 0$ . The basic assumption in Eq. (7) is that tube density  $\rho$  is very low, and therefore the tubes do not interact with each other. Consequently, the tube–tube contact parameter  $Bi_C$  is set to zero in the finite volume computations to obtain a direct comparison. Since the parameter  $Bi_S$  is not known a priori, its value is adjusted to match the results from EMA for a value of  $a_K = 0.25$  nm for  $k_S/k_t = 10^{-2}$ . The same value of  $Bi_S$  is used in all subsequent calculations for other  $k_S/k_t$  ratios in Fig. 11a. It is important to notice that there is only one free parameter,  $Bi_S$ , in our simulations, corresponding to the adjustable parameter  $a_K$  in EMA. A good match with the results of EMA is obtained for the case of  $Bi_C = 0$ . Calculations were also performed in Fig. 11a for  $Bi_C = 10$ , representing nearly-perfect contact. For high  $Bi_C$ , the numerically computed  $k_{eff}$  is observed to deviate substantially from the EMA prediction even for densities below the percolation threshold  $\rho_{th}$ . This deviation is significant for all but the highest  $k_S/k_t$  values ( $<10^{-2}$ ), and would therefore be significant for computations of electrical and thermal conductivities in CNT composites. This suggests that high aspect ratio tubes strongly interact with each other even at tube densities below  $\rho_{th}$  and that the

**Fig. 13** **a** Location and shape of the heat pulse at different time instants along the first CNT for (5, 0) chirality. The pulse generation starts at  $t = 0.0$  ps. **b** Location and shape of the heat pulse at different time instants in the second CNT, also of the same chirality

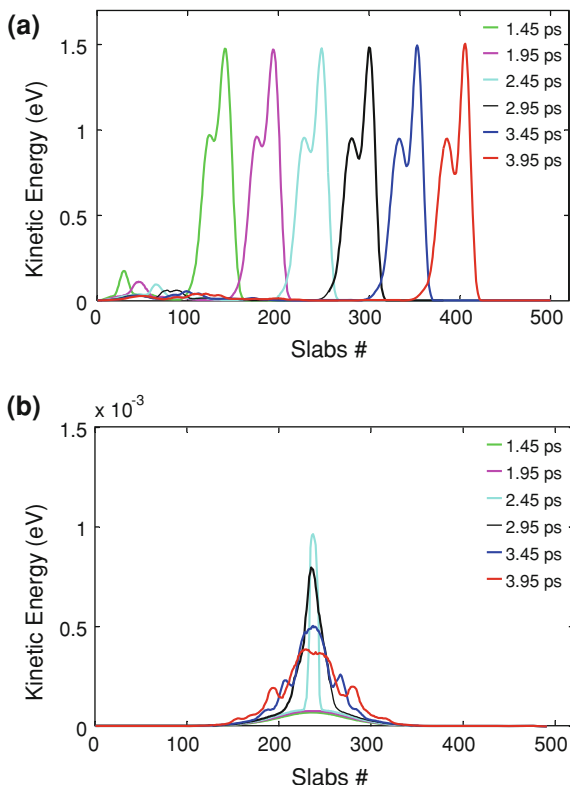


EMA is inadequate for the prediction of  $k_{eff}$  at all but the very lowest densities. Figure 11b presents the variation of  $k_{eff}$  with tube density with  $Bi_S$  as a parameter; the ratio  $(1/a_K)/Bi_S$  is held constant in the figure. A good match with EMA is found. The constant ratio  $(1/a_K)/Bi_S$  for different curves in Fig. 14.11b shows that the adjustable parameter in EMA,  $(1/a_K)$ , and that in the numerical calculations,  $Bi_S$ , are consistent. These results indicate that adjusting  $a_K$  to fit experimental data for  $\rho > \rho_{th}$  in previous studies [26, 57] adjusts in part for tube–tube interaction effects not present in EMA theory. These adjustments would tend to underpredict the true value of interface resistance, a claim also supported by Hung et al. [58].

## 5 Interfacial Thermal Transport Between Nanotubes

In the last two sections, we have considered conduction in a network of nanotubes and their composites where we have treated tube–tube and tube–substrate resistance values as parameters. Various experimental and numerical studies have been performed to analyze the interfacial energy transport and to estimate the thermal resistance between the CNTs and between the CNT and the substrate. In this section, we present our investigation of the thermal energy transport from one single-walled

**Fig. 14** **a** Location and shape of the heat pulse at different time instants along the first CNT for (7, 0) chirality. The pulse generation starts at  $t = 0.0$  ps. **b** Location and shape of the heat pulse at different time instants in the second CNT, also of the same chirality



nanotube (SWNT) to another SWNT positioned in a crossed configuration and subjected to an intense heat pulse using Molecular Dynamics (MD) techniques [59]. A schematic of two CNTs in a crossed configuration is shown in Fig. 12. Here, the CNTs are placed perpendicular to each other with a gap equal to a van der Waals distance of 3.4 Å. These CNTs are not covalently bonded at the interface.

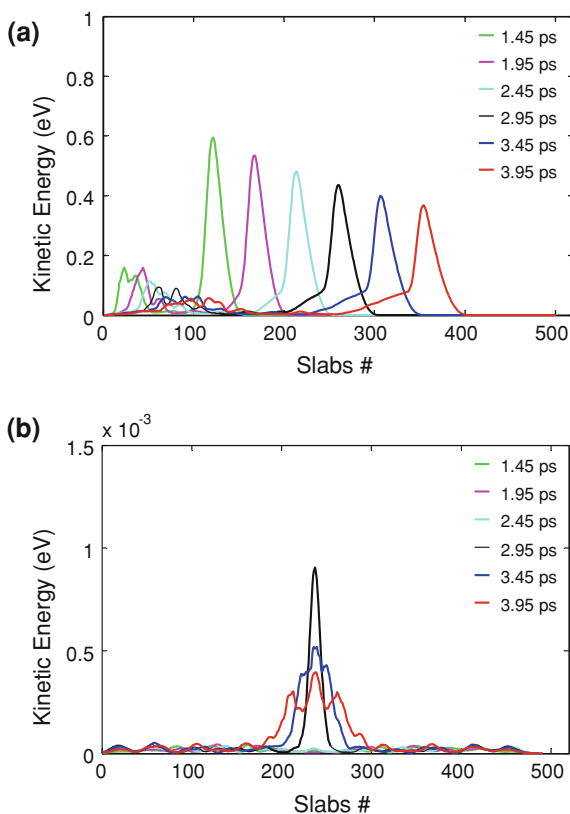
Selection of appropriate interatomic energies and forces is important for the reliability of classical MD simulations. We use the reactive empirical bond order (REBO) potential for C–C bond interaction and a truncated 12-6 type Lennard-Jones potential for non-bonded van der Waals interactions between CNTs. The REBO potential has been extensively applied to perform MD simulations in CNTs and CNTs in hydrocarbon composites/suspensions [33]. The analytical form of this potential is based on the intramolecular potential energy originally derived by Abell [60]. The REBO potential is given by:

$$U_{\text{REBO}} = \sum_i \sum_{i < j} [V_r(r_{ij}) - D_{ij} V_a(r_{ij})]. \quad (8)$$

where  $r_{ij}$  denotes the distance between atoms  $i$  and  $j$ ,  $V_r$  corresponds to interatomic core–core repulsive interactions, and  $V_a$  describes the attractive interactions due to the valence electrons. Here,  $D_{ij}$  corresponds to a many-body empirical bond-order



**Fig. 15** **a** Location and shape of the heat pulse at different time instants along the first CNT for (8, 0) chirality. The pulse generation starts at  $t = 0.0$  ps. **b** Location and shape of the heat pulse at different time instants in the second CNT, also of the same chirality



term. The 12-6 type LJ potential for non-bonded van der Waals interaction between individual carbon atoms is given as [38]:

$$U_{LJ} = 4\epsilon \left[ \left( \frac{\sigma}{r} \right)^{12} - \left( \frac{\sigma}{r} \right)^6 \right]. \quad (9)$$

Several different values of the energy and distance parameters in the L-J potential are considered for the interaction of C-C atoms in the CNT. The present study employs the parameterization used by Lukes et al., with  $\epsilon = 4.41$  meV and  $\sigma = 0.228$  nm. The details of the MD code used for the present analysis may be found in Ref. [60].

### 5.1 Heat Pulse Analysis Using Molecular Dynamics

MD simulations are used to examine transient heat pulse propagation in zig-zag tubes positioned in a crossed configuration for chiralities varying from (5, 0) to (10, 0). We generate the heat pulse at one end of the tube using the methodology

**Fig. 16 a** Location and shape of the heat pulse at different time instants along the first CNT for (10, 0) chirality. The pulse generation starts at  $t = 0.0$  ps. **b** Location and shape of the heat pulse at different time instants in the second CNT, also of the same chirality

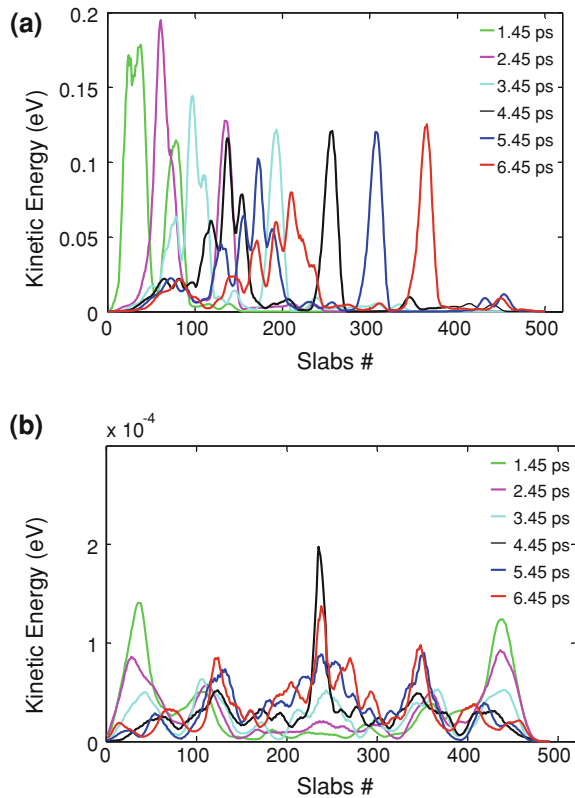


**Table 2** Pulse speed in the first tube and the maximum total energy rise in the second tube for different chiralities

CNT-Chirality	Pulse speed (km/s)	Increase in total energy of second tube until $t = 5.5$ ps (eV)
(5, 0)	22.0	0.129
(6, 0)	23.2	0.203
(7, 0)	22.6	0.046
(8, 0)	19.0	0.074
(10, 0)	12.5	0.037

proposed by Osman and Srivastava [61] for studying energy transport through a single CNT at low temperatures. In order to study heat pulse propagation in CNTs and to compare the results for different chiralities, each CNT is divided into 500 slabs along its axis (each slab is a ring). The length of each CNT is 106 nm, but the number of atoms in a slab depend on the chirality or diameter of the CNT, i.e., a single slab in a (5, 0), (6, 0), (7, 0), (8, 0) and (10, 0) CNT would have 10, 12, 14, 16, and 20 atoms respectively. One end of the first CNT, where the heat pulse is generated, is treated as a free boundary, while the other end is kept rigid

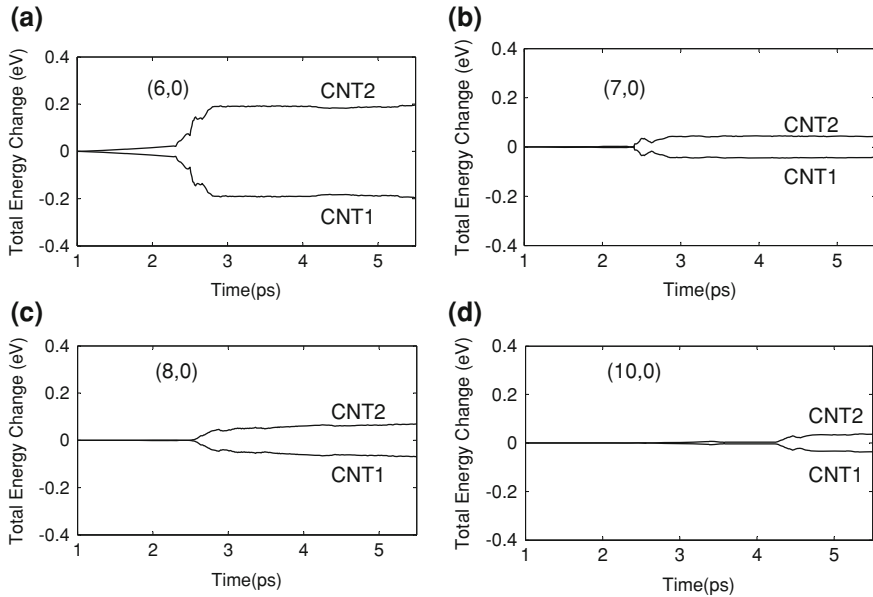
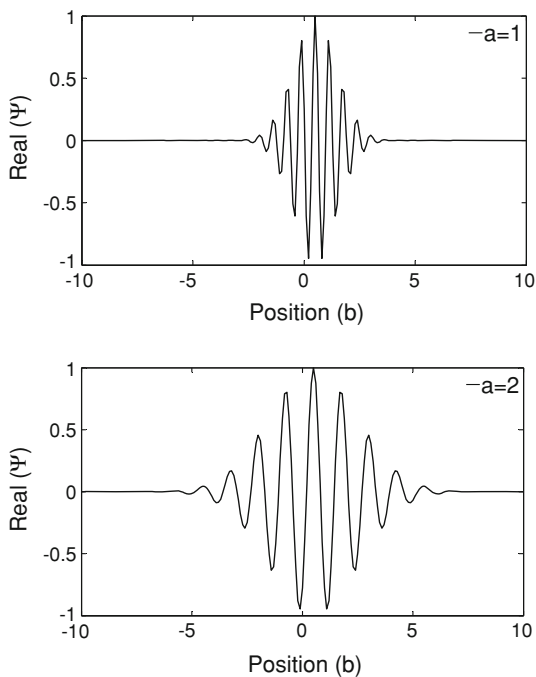


**Fig. 17** Change in total energy of CNTs as a function of time with reference total energy corresponding to  $t = 1$  ps. At  $t = 1$  ps, the pulse generated in CNT-1 starts propagating towards the contact region of the two CNTs. Here, CNT-1 corresponds to the CNT in which the pulse is generated; CNT-2 is located in a crossed-configuration with respect to CNT-1. The chirality of the CNTs is **a** (6, 0) **b** (7, 0) **c** (8, 0) and **d** (10, 0)

(see Fig. 12); both ends of the second CNT are held rigid. The boundary region of the first CNT (i.e., the CNT in which the pulse is generated) extends over 10 slabs. Before the generation of the heat pulse, both CNTs are quenched to a very low temperature of 0.01 K for 50,000 time steps (25 ps) to achieve thermal equilibrium at 0.01 K. Then, a strong heat pulse of one picosecond duration and a peak temperature of 800 K is generated at one end of the first CNT. The heat pulse is applied to 10 slabs near the left boundary using a Berendsen thermostat [62]. The heat pulse consists of a 0.05 ps rise time, a 0.9 ps duration with a constant temperature of 800 K, and a 0.05 ps fall time. During the 0.05 ps fall time, the temperature of the boundary slabs is decreased to reach a final temperature of 0.01 K and then held constant at that temperature for the rest of the simulation. This is done to prevent the exchange of large amounts of energy from the boundary slabs to the region of interest after the generated pulse has started propagating towards the right boundary of the first CNT.

Our analysis is focused on the time window from the point of generation of the pulse to the time before heat pulse reaches the right boundary to avoid the effects of boundary reflection. The temperature of each slab is spatially averaged over ten slabs centered at the slab of interest. In our simulations, the temperature is

**Fig. 18** An example of a Morlet wavelet with different values of the scale  $a$  [65]



time-averaged over sets of 200 time steps ( $\sim 100$  fs) to reduce the effect of statistical fluctuations and is recorded during the entire simulation time. The speed of the pulse is determined from the spatial distance traversed by the particular pulse during a given time interval.

We first study the interaction between two CNTs in a crossed configuration when a heat pulse is passed through first CNT using the methodology described in the above sections. Our interest is in analyzing the energy transfer to the second tube when the heat pulse passes through the contact zone, and also to study the waves generated in the second tube due to this energy transfer. The distance between the CNTs remains in the range of 3–3.7 Å during the entire simulation for CNTs of chirality (5, 0), (6, 0) and (7, 0). For CNTs of chirality (8, 0), this distance remains in the range of 4–4.5 Å, while for CNTs of chirality (10, 0), it remains in the range of 5–5.5 Å.

The location and shape of the heat pulses at different time instants along the first and second CNTs for the case of (5, 0) chirality are shown in Fig. 13a, b respectively. The amplitude of the heat pulses is presented in terms of the average kinetic energy of the atoms in ten slabs at any location. Here,  $t = 0$  ps corresponds to the time when heat pulse generation has started at the left end of the first CNT. The attenuation in peak kinetic energy ( $\sim 1.2$  eV) of the heat pulse is negligible and it is seen to propagate like a ballistic pulse along the first tube. This pulse moves with a speed of 22 km/s along the nanotube, which is very close to the speed of sound (20.3 km/s) associated with longitudinal acoustic (LA) phonon

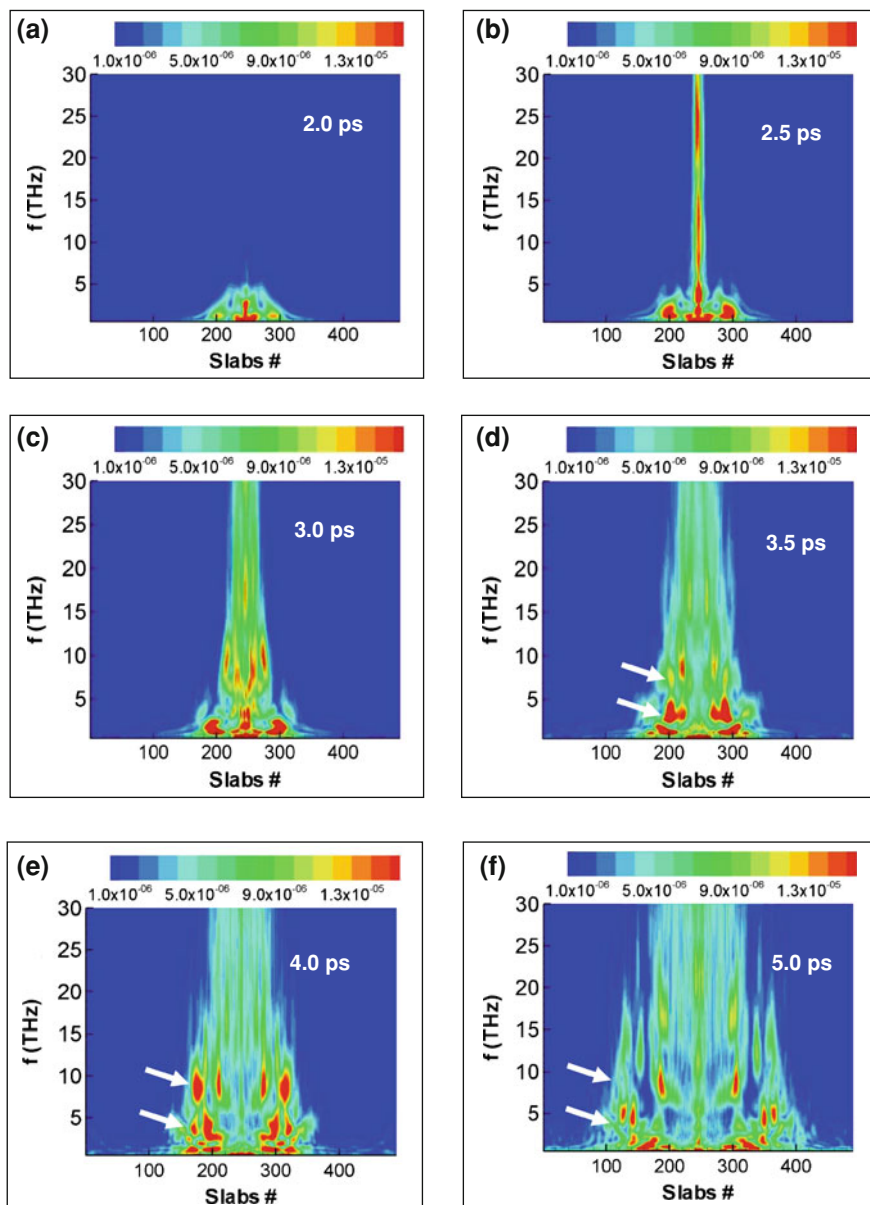


**Fig. 19** Frequency spectrum along the second nanotube for (5, 0) chirality at different time instants. **a** 2.0 ps. **b** 2.5 ps. **c** 3.0 ps. **d** 3.5 ps. **e** 4.0 ps. **f** 5.0 ps. *White arrows* shows frequencies corresponding to 5 and 10 THz

waves in zig-zag nanotubes [62]. Two CNTs located in a crossed configuration make contact at their mid-point, which is at 53 nm from their free ends. When the heat pulse in the first tube approaches this contact zone, the kinetic energy in the

other tube increases at the location of the contact, Fig. 13b. The kinetic energy reaches its maximum at  $t = 2.6$  ps which is approximately the time taken by the heat pulse in the first tube to cross the contact zone. The peak kinetic energy in the second tube is 1.5 meV, which is very low in comparison to peak kinetic energy of 1.2 eV of the heat pulse in the first tube. This indicates that coupling is very weak between two CNTs for these fast moving pulses, since little time is spent by the pulse in the contact zone. The energy given to the second tube at the point of contact spreads along the second tube. This is indicated by the decreasing kinetic energy at the center of the second tube and the symmetrically excited heat pulses on both sides of the contact in Fig. 13b. The speed of propagation of the excited heat pulse in the second tube is very low and it is difficult to relate these pulses with any specific phonon mode by observing their transient propagation profiles.

We perform a similar heat pulse analysis for nanotubes of chirality (6, 0), (7, 0), (8, 0) and (10, 0); the shape and location of the heat pulse along the nanotube for different time instants for the (7, 0), (8, 0) and (10, 0) chiralities are shown in Figs. 14, 15 and 16. It is observed that the behavior of heat pulses in the nanotubes is very dependent on the chirality or the diameter of the tube. The speed of heat pulse propagation in the first tube and the increase in kinetic energy in the second tube until  $t = 5.5$  ps are listed in Table 2. Heat pulse propagation in the first tube for (6, 0) and (7, 0) chiralities is similar to that for the (5, 0) nanotube, i.e., the heat pulse propagates like a ballistic wave with a speed in the range of 22–23 km/s. However, the pulses excited in the second tube are significantly different for different chirality tubes. No conclusions can be drawn merely by looking at the kinetic energy rise in the second tube (see Table 2). However, it can be observed that heat spreading along the second tube is faster in the (5, 0) tube in comparison to the (6, 0) and (7, 0) tubes (see Figs. 13, 14). It is also observed that the kinetic energy at the centre of the second tube drops relatively fast in the (6, 0) tube in comparison to the (7, 0) tube.

Heat pulse propagation is completely different for (8, 0) and higher chirality tubes. For the (8, 0) tube, the heat pulse decays while propagating along the first tube and also broadens with time, a behavior which is completely different from that observed in low chirality tubes. At time  $t = 1.45$  ps, the peak kinetic energy of the pulse is 0.68 eV, and decays to 0.42 eV at  $t = 3.95$  ps, Fig. 15a. The pulse speed in the (8, 0) tube is 19 km/s, which is lower than the pulse speed observed in lower chirality tubes (see Table 2). Oman and Srivastava [61] observed a similar decay in the pulse speed in zig-zag tubes for twisting phonon modes (TW) with speed ranging in 16–18 km/s. The pulse excited in the second tube also shows different characteristics, and exhibits a pulse shape which is more flat at the center, Fig. 15b. All these behaviors imply a dissipative nature to the pulse propagation in (8, 0) tubes.

Heat pulse propagation in a (10, 0) tube is much different from the low chirality tubes previously discussed. The high kinetic energy in the heat pulse in the first tube cannot be sustained and the pulse decays very quickly. At  $t = 2.45$  ps, a clearly identifiable wave shape evolves from the dissipating heat pulse; the speed of this wave is 12.5 km/s, which corresponds to the second sound wave speed

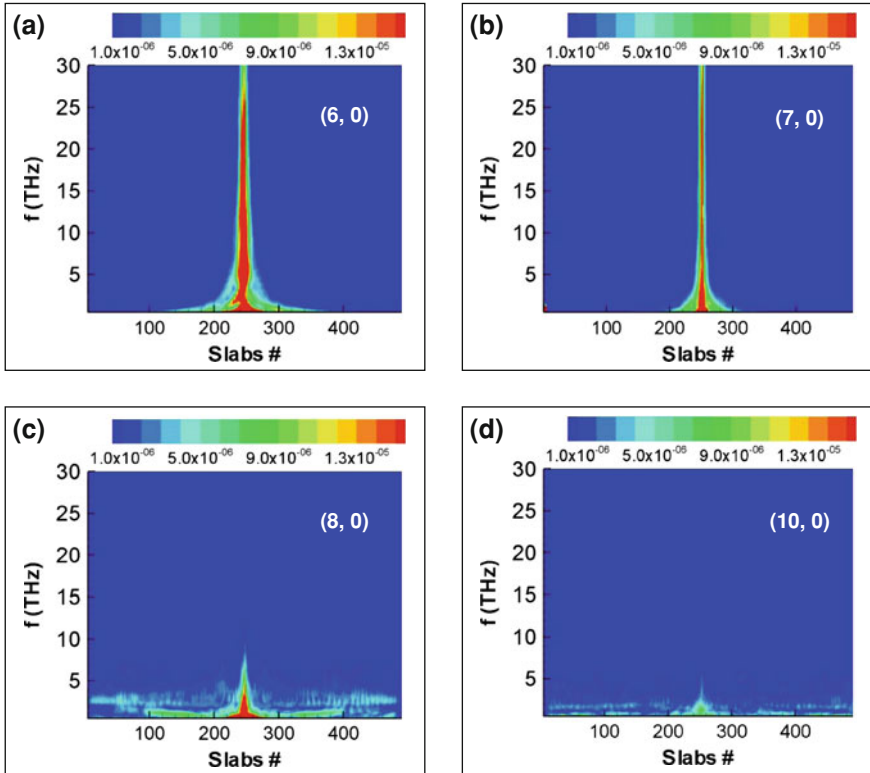


**Fig. 20** Frequency spectrum along the second CNT at 2.5 ps for chirality **a** (6, 0). **b** (7, 0). **c** (8, 0). **d** (10, 0)

observed in zig-zag tubes in Ref. [61]. In transient experiments, at low temperatures and in structures with high purity, normal phonon scattering processes can play an important role. They may couple various phonon modes and make possible the collective oscillation in phonon density which is second sound. Second sound is observed under very restrictive conditions [61]. One of these conditions is that the momentum conserving normal phonon scattering processes should be dominant compared to the momentum randomizing Umklapp phonon scattering processes [61]. For CNTs, thermal conductivity increases even up to room temperature and it can reasonably be believed that N-process phonon interactions dominate over a wide range of temperature. These arguments and the observed speed of the wave ( $12.5 \text{ km/s} = 1/3^{0.5}$  times the LA phonon speed) suggest that the observed wave pulse in the (10, 0) nanotube corresponds to that of second sound.

The peak kinetic energy of the second sound wave mode observed in (10, 0) tube is 0.12 eV, which is much smaller than the peak kinetic energy of leading heat pulses observed in the low-chiral tube configurations. In addition, due to the

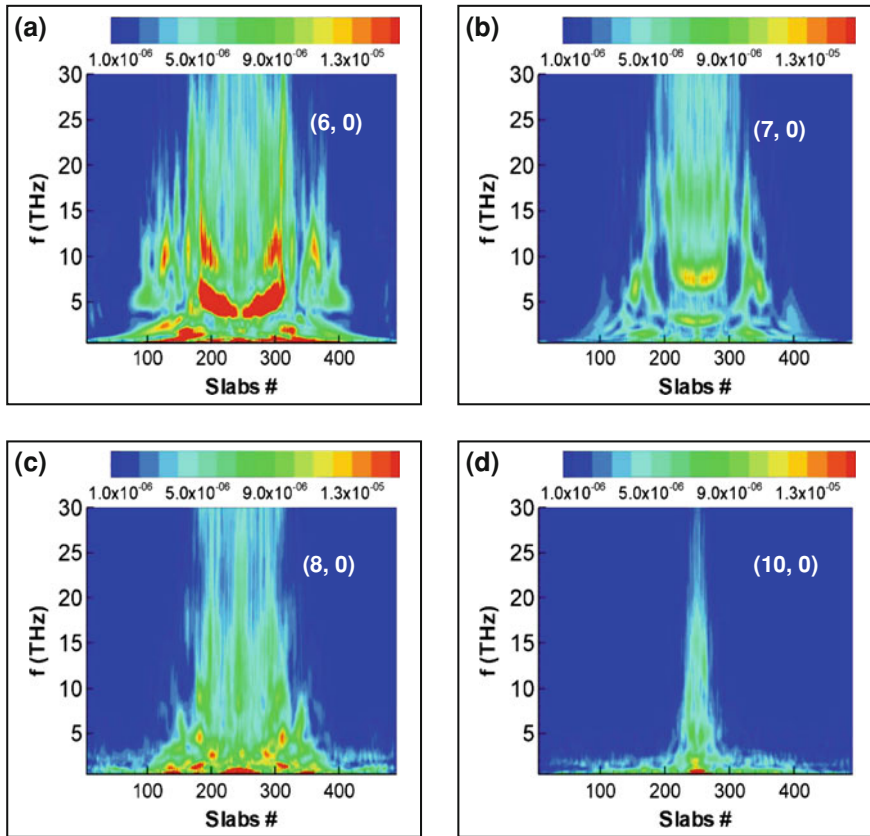


**Fig. 21** Frequency spectrum along the second CNT at 5.0 ps for chirality **a** (6, 0), **b** (7, 0), **c** (8, 0), **d** (10, 0)

low speed, this pulse in the first CNT does not cross the contact zone in 4 ps (this is the time range for which we analyzed low-chirality tubes), so we have extended the analysis up to 6.5 ps. The energy gained by the second CNT due to the interaction with the heat pulse of the first CNT is very low. This is the reason for a very small rise in the peak kinetic energy ( $\sim 0.2$  meV) of the excited pulse in the second tube, Fig. 16b. The kinetic energy of the carbon atoms located at the contact area of the second CNT (black and red curves in Fig. 16b) is of the same order as that of the kinetic energy of atoms at other locations (see peaks at the CNT ends in Fig. 16b). From our analysis, we have observed that in low-chirality CNTs we can generate a purely ballistic pulse, while in high-chirality CNTs, a diffusive tail is also present and the pulse cannot sustain its peak temperature during propagation. We see a difference between our results and Osman and Srivastava's results only for low-chirality CNTs.



The change in total energy of the CNTs as a function of time is plotted in Fig. 17 for (6, 0), (7, 0), (8, 0) and (10, 0) tubes. The change in total energy is computed with respect to the reference total energy at  $t = 1$  ps; this is time at which the pulse generated in the first CNT starts propagating towards the contact region of the two CNTs. The magnitude of total energy exchange or increase in total energy of the second tube up to time instant 5.5 ps is presented in Table 2 for tubes of different chiralities. The energy exchange between the tubes is largest for the (6, 0) tube and decreases for high-chirality tubes, Fig. 17. However a definitive statement regarding this cannot be made based on the present analysis as the energy exchange for the (5, 0) tube is lower than that for the (6, 0) tube by 0.07 eV and the energy exchange for the (7, 0) tube is lower than that for the (8, 0) tube by 0.028 eV. The above analysis shows that lower-chirality tubes have better coupling in comparison to high- chirality tubes as far as these heat pulses are concerned.

Phonon modes with high speed are very inefficient in transferring energy to the second tube as they spend very little time in the contact zone. Thus, it is likely that for realistic applications, slow-moving phonon modes (for example, optical modes) in the first CNT would be better-coupled to the second CNT. Shiomi and Maruyama [63] observe from their modal analyses on a single tube using wavelet transformations that the major contribution to non-Fourier heat conduction comes from optical phonon modes with sufficient group velocity and with wave vectors in the intermediate regime for short nanotubes. Dispersion curves for CNTs of chirality (5, 5) show that even at low frequencies, longitudinal and transverse optical modes may be present, with velocities comparable with the acoustic modes. In a nanotube network, the link between two nanotubes is of the order of just few nanometers. Therefore, in nanotube networks where the contact between the tubes governs the transport, optical phonon modes may be a dominant heat transfer pathway for communication between tubes.

## 5.2 Wavelet Analysis of Heat Pulse

Wavelet analysis of the heat pulse excited in the CNT configuration described in the previous section (see Fig. 12) is performed for different chiralities of the tubes. The wavelet transform (WT) is an analysis tool well-suited for the study of processes which occur over finite spatial and temporal domains. The wavelet transform is a generalized form of the Fourier transform (FT). A WT uses generalized local functions known as wavelets which can be stretched and translated with a desired resolution in both the frequency and time domains [64, 65].

Wavelets decompose a time series in the time–frequency space and are useful for identifying the evolution of dominant frequency modes with time. A time signal  $s(t)$  is decomposed using wavelet methods in terms of the elementary function  $\psi_{b,a}$  derived from a mother wavelet  $\psi$  by dilation and translation [64]:

$$\psi_{b,a}(t) = \frac{1}{a^{0.5}} \psi \left( \frac{t-b}{a} \right). \quad (10)$$

Here,  $a$  and  $b$  are parameters which control dilation and translation respectively. The  $a$  parameter is also known as the *scale* in wavelet analysis.  $\psi_{b,a}$  is known as the *daughter* wavelet as it is derived from the mother wavelet  $\psi$  using translation and dilation. The normalization factor  $a^{0.5}$  ensures that the mother and daughter wavelets have the same energy. The wavelet transform (WT) of a signal  $s(t)$  is given as the convolution integral of  $s(t)$  with  $\psi^*$ , where  $\psi^*$  is the complex conjugate of the wavelet function  $\psi$ :

$$W(b, a) = \frac{1}{a^{0.5}} \int \psi^* \left( \frac{t-b}{a} \right) s(t) dt. \quad (11)$$

In general, wavelet functions are complex functions, so the  $wt$  are also complex, and have a real part, an imaginary part and a phase angle. The power spectrum of a WT is defined as  $|W|^2$ . We use the Morlet wavelet for heat pulse analysis; this wavelet has the form of a plane wave with a Gaussian envelope [64]. The Morlet wavelet is given by:

$$\psi = e^{iwt} \times e^{-0.5|t|^2}. \quad (12)$$

The form of this wavelet is shown in Fig. 18 after translating by different values of  $b$  and dilating by different values of the scale parameter  $a$ .

The power spectrum of the velocity magnitude of each atom in the nanotube is computed using the method described above. By summing the power spectrum over all the atoms of one ring, a one-dimensional projection of the temporal spectra along the nanotube axis is obtained. In this way, temporally evolving spectra of the velocity magnitude for the entire spatio-temporal field are obtained.

Wavelet analysis of the energy modes excited in the second CNT due to the interaction with first CNT is performed for chirality of tubes varying from (5, 0) to (10, 0). The power spectrum of the velocity magnitude of each atom in the nanotube is computed using the method described above. Temporally evolving spectra of the velocity magnitude for the entire spatio-temporal field are computed. Results are presented as temporal sequences of the spectral contours in the frequency-space domain in Fig. 19 for a (5, 0) CNT. Six temporal sequences are used, which correspond to  $t = 2.0, 2.5, 3.0, 3.5, 4.0$  and  $5.0$  ps. In these plots, the vertical axis represents the frequency in THz and the horizontal axis represents the spatial location along the nanotube axis in terms of the slab (i.e. ring) numbers.

The evolution and propagation of spectral modes along the tube axis for a (5, 0) CNT at different time instants may be observed in Fig. 19. At  $t = 2$  ps, the heat pulse in the first tube is approaching the contact zone, Fig. 19a; thus some low frequency phonon modes are excited in the second nanotube at the location of the contact. At  $t = 2.5$  ps (Fig. 19b), the heat pulse in the first tube crosses the contact zone; this is the time at which the peak temperature of the thermal pulse excited in the second CNT is observed (Fig. 13b). Phonon modes of frequencies up

to 30–35 THz are excited in the second nanotube by this time, but most of the dominant frequencies are less than 10 THz, Fig. 19b. Once the heat pulse in the first tube moves away from the contact zone, the energy given to the second tube spreads to both sides of the tube symmetrically. Different phonon modes are excited along the second tube, and can be observed from the contour plots in Fig. 19c–f. The contour plot at  $t = 3.0$  ps shows two distinctly visible modes, one centered around 5 THz and another centered around 10 THz. The speed of these modes may be computed from the movement of the high power spectrum color patches corresponding to these frequencies along the nanotube axis in the contour plot. The computed speed is 12.0 km/s, which is close to the speed of the second sound waves observed in these zig-zag tubes [61]. These color patches are shown in Fig. 19d–f by white arrows. Most of the other dominant modes correspond to frequencies even lower than 5 THz, which is in correspondence with the small amount of heat transferred to the second tube from the heat pulse in the first tube.

Contours of the power spectrum for (6, 0), (7, 0), (8, 0) and (10, 0) CNTs at  $t = 2.5$  ps and 5.0 ps are shown in Figs. 20, 21 respectively. As in the case of the (5, 0) CNT, two dominant phonon modes corresponding to 5 and 21 THz are seen to propagate along the second tube for (6, 0) and (7, 0) CNTs, Fig. 21a, b. These contour plots also clearly show that the rate of heat spreading along the CNT axis slows down with increasing diameter. This is also observed in the heat pulse analysis in the previous section by examining the location and shape of the heat pulses generated in the second tube. A similar comparison cannot be made for (8, 0) and (10, 0) CNTs because the pulse generated in the first CNT is not sustained at its initial peak temperature, and very little heat is transferred to the second CNT for these cases. The spectral modes for the (10, 0) CNT are completely different from other CNTs; most of the high energy modes present in low-chirality CNTs are not excited, Fig. 21d. This is due to the evolution of second sound waves in the first CNT; the peak temperature is an order of magnitude lower than that in low chirality CNTs, Figs. 16b, 21d.

## 6 Conclusions

In summary, a computational model for thermal and electrical transport in nanotube composites has been developed and applied to the determination of lateral electrical and thermal conductivity of finite thin films. The model has been verified against analytical solutions, and validated against experimental data for tube densities above and below the percolation threshold, for nanotube networks in the absence of a substrate, as well as for nanotube-plastic and nanotube-organic composites. Excellent matches with experimental data have established the general validity of the model and provided much deeper insights into electrical and thermal transport in these non-classical materials. This understanding not only advances the relevance of percolation theory to broader class of problems, but

will also help design and optimization of these materials for future technological applications.

Nevertheless, a number of important issues remain to be addressed. The model employs thermal contact parameters  $Bi_c$ ,  $Bi_s$ , and electrical contact parameters  $c_{ij}$  and  $d_{is}$ , which are at present unknown. These must be determined either from careful experiments or from atomistic simulations of tube–tube and tube-substrate contact. Furthermore, while the thermal conductivities of individual freestanding nanotubes and nanowires has been measured and modeled, the modification of these values for tubes and wires encased in plastic or organic substrates is not well understood. Ultimately, our interest is not only in the simulation of conductivity but also in the coupled electro-thermal analysis and design of flexible large-area electronics. We have focused on the analysis of the lateral thermal conductivity of the composite, but normal thermal conductivity of the composite is also of great importance from the perspective of heat removal from the device and merits a detailed investigation.

In this chapter, we also analyzed the thermal transport between two CNTs for different chiralities using the MD technique and the wavelet method. A thermal pulse was generated at one end of the first CNT to study the response of the second tube when this pulse passed the contact region of the two CNTs. The results of our heat pulse studies demonstrate that phonon modes with high speed are very inefficient in transferring energy to the second tube as they spend very little time in the contact zone. Most likely, slow-moving phonon modes in the first CNT would be better coupled to the second CNT and would dominate thermal boundary conductance between these CNTs. To better understand the coupling of modes between tubes, a wave packet corresponding to specific phonon modes should be passed through a CNT and its interaction with other CNTs should be studied. Understanding the coupling between CNTs of different chirality and contact area could also be of great interest for engineering the properties of CNT-network based composites. Most of the present work is in the low temperature regime. It is also important to investigate transport mechanisms in the high temperature regime using either appropriate numerical modeling or experimental techniques.

**Acknowledgments** Support of J. Murthy and S. Kumar under NSF grants CTS-0312420, CTS-0219098, EE-0228390, the Purdue Research Foundation and Purdue's Network for Computational Nanotechnology (NCN) is gratefully acknowledged. M. A. Alam acknowledges support from the Focus Center Research Program (FCRP-MSD).

## References

1. Hur, S.H., Kocabas, C., Gaur, A., et al.: Printed thin-film transistors and complementary logic gates that use polymer-coated single-walled carbon nanotube networks. *J. Appl. Phys.* **98**(11), 114302 (2005)
2. Reuss, R.H., Chalamala, B.R., Moussessian, A., et al.: Macroelectronics: perspectives on technology and applications. *Proc. IEEE* **93**(7), 1239–1256 (2005)

3. Collins, P.C., Arnold, M.S., Avouris, P.: Engineering carbon nanotubes and nanotube circuits using electrical breakdown. *Science* **292**(5517), 706–709 (2001)
4. Kagan, C.R., Andry, P.: *Thin film transistors*. Marcel Dekker, New York (2003)
5. Novak, J.P., Snow, E.S., Houser, E.J., et al.: Nerve agent detection using networks of single-walled carbon nanotubes. *Appl. Phys. Lett.* **83**(19), 4026–4028 (2003)
6. Alam M.A. Nair P.R.: Geometry of diffusion and the performance limits of nanobiosensors. *Nanotechnology 501 lecture series*. [https://www.nanohub.org/resources/2048/\(2006\)](https://www.nanohub.org/resources/2048/(2006))
7. Madelung, O.: *Technology and applications of amorphous silicon*. Springer, Berlin (2000)
8. Zhou, Y.X., Gaur, A., Hur, S.H., et al.: P-channel, n-channel thin film transistors and p-n diodes based on single wall carbon nanotube networks. *Nano Lett.* **4**(10), 2031–2035 (2004)
9. Snow, E.S., Campbell, P.M., Ancona, M.G., et al.: High-mobility carbon-nanotube thin-film transistors on a polymeric substrate. *Appl. Phys. Lett.* **86**(3), 066802 (2005)
10. Snow, E.S., Novak, J.P., Lay, M.D., et al.: Carbon nanotube networks: nanomaterial for macroelectronic applications. *J. Vac. Sci. Technol. B* **22**(4), 1990–1994 (2004)
11. Snow, E.S., Novak, J.P., Campbell, P.M., et al.: Random networks of carbon nanotubes as an electronic material. *Appl. Phys. Lett.* **82**(13), 2145–2147 (2003)
12. Cao, Q., Rogers, J.A.: Ultrathin films of single-walled carbon nanotubes for electronics and sensors: A review of fundamental and applied aspects. *Adv. Material* **21**(1), 29–53 (2009)
13. Kumar, S., Murthy, J.Y., Alam, M.A.: Percolating conduction in finite nanotube networks. *Phys. Rev. Lett.* **95**(6), 066802 (2005)
14. Hur, S.H., Khang, D.Y., Kocabas, C., et al.: Nanotransfer printing by use of noncovalent surface forces: applications to thin-film transistors that use single-walled carbon nanotube networks and semiconducting polymers. *Applied Physics Letters* **85**(23), 5730–5732 (2004)
15. Kocabas, C., Hur, S.H., Gaur, A., et al.: Guided growth of large-scale, horizontally aligned arrays of single-walled carbon nanotubes and their use in thin-film transistors. *Small* **1**(11), 1110–1116 (2005)
16. Kocabas, C., Shim, M., Rogers, J.A.: Spatially selective guided growth of high-coverage arrays and random networks of single-walled carbon nanotubes and their integration into electronic devices. *J. Am. Chem. Soc.* **128**(14), 4540–4541 (2006)
17. Milton, G.W.: *The theory of composites*. Cambridge University Press, New York (2002)
18. Nan, C.W., Birringer, R., Clarke, D.R., et al.: Effective thermal conductivity of particulate composites with interfacial thermal resistance. *J. Appl. Phys.* **81**(10), 6692–6699 (1997)
19. Jeong, C., Nair, P., Khan, M., Lundstrom M., Alam, M.A.: Prospects for Nanowire-doped polycrystalline graphene films for ultratransparent, highly conductive electrodes. *Nano Lett.* **11** (11), 5020–5025 (2011)
20. Cao, Q., Kim, H. K., Pimparkar, N., et al.: Medium-scale carbon nanotube thin-film integrated circuits on flexible plastic substrates. *Nature* **454**, 495–500, (2008)
21. Kumar, S., Alam, M.A., Murthy, J.Y.: Computational model for transport in nanotube-based composites with applications to flexible electronics. *ASME J. Heat Transf.* **129**(4), 500–508 (2007)
22. Kumar, S., Pimparkar, N., Murthy, J.Y., et al.: Theory of transfer characteristics of nanotube network transistors. *Appl. Phys. Lett.* **88**, 123505 (2006)
23. Zhang, G., Qi, P., Wang, X., et al.: Selective etching of metallic carbon nanotubes by gas-phase reaction. *Science* **314**, 974–977 (2006)
24. Arnold, M.S., Green, A.A., Hulvat, J.F., et al.: Sorting carbon nanotubes by electronic structure using density differentiation. *Nat. Nanotechnol.* **1**, 60–65 (2006)
25. Huang, H., Liu, C., Wu, Y., et al.: Aligned carbon nanotube composite films for thermal management. *Adv. Material* **17**, 1652–1656 (2005)
26. Nan, C.W., Liu, G., Lin, Y.H., et al.: Interface effect on thermal conductivity of carbon nanotube composites. *Appl. Phys. Lett.* **85**(16), 3549–3551 (2004)
27. Biercuk, M.J., Llaguno, M.C., Radosavljevic, M., et al.: Carbon nanotube composites for thermal management. *Appl. Phys. Lett.* **80**(15), 2767–2769 (2002)

28. Xu, X.J., Thwe, M.M., Shearwood, C., et al.: Mechanical properties and interfacial characteristics of carbon-nanotube-reinforced epoxy thin films. *Appl. Phys. Lett.* **81**(15), 2833–2835 (2002)
29. Reibold, M., Paufler, P., Levin, A.A., et al.: Carbon nanotubes in an ancient Damascus sabre. *Nature* **444**(16), 286 (2006)
30. Hu, L., Hecht, D.S., Gruner, G.: Percolation in transparent and conducting carbon nanotube networks. *Nano Lett.* **4**(12), 2513–2517 (2004)
31. Koblinski, P., Cleri, F.: Contact resistance in percolating networks. *Phys. Rev. B* **69**(18), 184201 (2004)
32. Hu, T., Grosberg, A.Y., Shklovskii, B.I.: Conductivity of a suspension of nanowires in a weakly conducting medium. *Phys. Rev. B* **73**(15), 155434 (2006)
33. Lukes, J.R., Zhong, H.L.: Thermal conductivity of individual single-wall carbon nanotubes. *J. Heat Transf.-Trans. ASME* **129**(6), 705–716 (2007)
34. Maruyama, S., Igarashi, Y., Shibuta, Y.: Molecular dynamics simulations of heat transfer issues in carbon nanotubes. In: *The 1st international symposium on micro & nano technology*. Honolulu, Hawaii, USA 2004
35. Small, J.P., Shi, L., Kim, P.: Mesoscopic thermal and thermoelectric measurements of individual carbon nanotubes. *Solid State Commun.* **127**(2), 181–186 (2003)
36. Maune, H., Chiu, H.Y., Bockrath, M.: Thermal resistance of the nanoscale constrictions between carbon nanotubes and solid substrates. *Appl. Phys. Lett.* **89**(1), 013109 (2006)
37. Carlborg, C.F., Shiomi, J., Maruyama, S.: Thermal boundary resistance between single-walled carbon nanotubes and surrounding matrices. *Phys. Rev. B* **78** (20), 205406 (2008)
38. Zhong, H.L., Lukes, J.R.: Interfacial thermal resistance between carbon nanotubes: molecular dynamics simulations and analytical thermal modeling. *Phys. Rev. B* **74**(12), 125403 (2006)
39. Greaney, P.A., Grossman, J.C.: Nanomechanical energy transfer and resonance effects in single-walled carbon nanotubes. *Phys. Rev. Lett.* **98**(12), 125503 (2007)
40. Prasher, R.S., Hu, X.J., Chalopin, Y., et al.: Turning carbon nanotubes from exceptional heat conductors into insulators. *Phys. Rev. Lett.* **102**, 105901 (2009)
41. Pimparkar, N., Kumar, S., Murthy, J.Y., et al.: Current–voltage characteristics of long-channel nanobundle thin-film transistors: A ‘bottom-up’ perspective. *IEEE Electron Device Lett.* **28**(2), 157–160 (2006)
42. Bo, X.Z., Lee, C.Y., Strano, M.S., et al.: Carbon nanotubes-semiconductor networks for organic electronics: The pickup stick transistor. *Appl. Phys. Lett.* **86**(18), 182102 (2005)
43. Kumar, S., Blanchet, G.B., Hybertsen, M.S., et al.: Performance of carbon nanotube-dispersed thin-film transistors. *Appl. Phys. Lett.* **89**(14), 143501 (2006)
44. Kundert, K.S.: *Sparse user’s guide*, Department of Electrical Engineering and Computer Sciences, University of California, Berkeley, CA, USA (1988)
45. Pike, G.E., Seager, C.H.: Percolation and conductivity—computer study 0.1. *Phys. Rev. B* **10**(4), 1421–1434 (1974)
46. Alam, M.A.: Nanostructured electronic devices: Percolation and reliability. Intel-purdue summer school on electronics from bottom up. <http://nanohub.org/resources/7168> (2009)
47. Foygel, M., Morris, R.D., Anez, D., et al.: Theoretical and computational studies of carbon nanotube composites and suspensions: electrical and thermal conductivity. *Phys. Rev. B* **71**(10), 104201 (2005)
48. Shenogina, N., Shenogin, S., Xue, L., et al.: On the lack of thermal percolation in carbon nanotube composites. *Appl. Phys. Lett.* **87**(13), 133106 (2005)
49. Frank, D.J., Lobb, C.J.: Highly efficient algorithm for percolative transport studies in 2 dimensions. *Phys. Rev. B* **37**(1), 302–307 (1988)
50. Lobb, C.J., Frank, D.J.: Percolative conduction and the Alexander-Orbach conjecture in 2 dimensions. *Phys. Rev. B* **30**(7), 4090–4092 (1984)
51. Pimparkar, N., Alam, M.A.: A “bottom-up” redefinition for mobility and the effect of poor tube–tube contact on the performance of CNT nanonet thin-film transistors. *IEEE Electron Device Lett.* **29**(9), 1037–1039 (2008)

52. Taur, Y., Ning, T.: *Fundamentals of modern VLSI devices*. Cambridge University Press, New York (1998)
53. Fuhrer, M.S., Nygard, J., Shih, L., et al.: Crossed nanotube junctions. *Science* **288**(5465), 494–497 (2000)
54. Seidel, R.V., Graham, A.P., Rajasekharan, B., et al.: Bias dependence and electrical breakdown of small diameter single-walled carbon nanotubes. *J. Appl. Phys.* **96**(11), 6694–6699 (2004)
55. Huxtable, S.T., Cahill, D.G., Shenogin, S., et al.: Interfacial heat flow in carbon nanotube suspensions. *Nat. Material* **2**(11), 731–734 (2003)
56. Kumar, S., Alam, M.A., Murthy, J.Y.: Effect of percolation on thermal transport in nanotube composites. *Appl. Phys. Lett.* **90**(10), 104105 (2007)
57. Bryning, M.B., Milkie, D.E., Islam, M.F., et al.: Thermal conductivity and interfacial resistance in single-wall carbon nanotube epoxy composites. *Appl. Phys. Lett.* **87**(16), 161909 (2005)
58. Hung, M.T., Choi, O., Ju, Y.S., et al.: Heat conduction in graphite-nanoplatelet-reinforced polymer nanocomposites. *Appl. Phys. Lett.* **89**(2), 023117 (2006)
59. Kumar, S., Murthy, J.Y.: Interfacial thermal transport between nanotubes. *J. Appl. Phys.* **106**(8), 084302 (2009)
60. Brenner, D.W., Shenderova, O.A., Harrison, J.A., et al.: A second-generation reactive empirical bond order (rebo) potential energy expression for hydrocarbons. *J. Phys.-Condens. Matt.* **14**(4), 783–802 (2002)
61. Osman, M.A., Srivastava, D.: Molecular dynamics simulation of heat pulse propagation in single-wall carbon nanotubes. *Phys. Rev. B* **72**(12), 125413 (2005)
62. Erhart, P., Albe, K.: The role of thermostats in modeling vapor phase condensation of silicon nanoparticles. *Appl. Surf. Sci.* **226**(1–3), 12–18 (2004)
63. Maruyama, S.J.: Non-Fourier heat conduction in a single-walled carbon nanotube: classical molecular dynamics simulations. *Phys. Rev. B* **73**(20), 205420 (2006)
64. Lau, K.M., Weng, H.: Climate signal detection using wavelet transform: How to make a time series sing. *Bull. Am. Meteorol. Soc.* **76**(12), 2391–2402 (1995)
65. Torrence, C., Compo, G.P.: A practical guide to wavelet analysis. *Bull. Am. Meteorol. Soc.* **79**(1), 61–78 (1998)
66. Liu, C.H., Huang, H., Wu, Y., et al.: Thermal conductivity improvement of silicone elastomer with carbon nanotube loading. *Appl. Phys. Lett.* **84**(21), 4248–4250 (2004)
67. Gong, Q.M., Li, Z., Bai, X.D., et al.: Thermal properties of aligned carbon nanotube/carbon nanocomposites. *Materials Science and Engineering a-Structural Materials Properties Microstructure and Processing* **384**(1–2), 209–214 (2004)
68. Choi, S.U.S., Zhang, Z.G., Yu, W., et al.: Anomalous thermal conductivity enhancement in nanotube suspensions. *Appl. Phys. Lett.* **79**(14), 2252–2254 (2001)
69. Wen, D.S., Ding, Y.L.: Effective thermal conductivity of aqueous suspensions of carbon nanotubes (carbon nanotubes nanofluids). *J. Thermophy. Heat Transf.* **18**(4), 481–485 (2004)